THESIS FOR THE DEGREE OF DOCTOR OF PHILOSOPHY

Temporal Characteristics of Boreal Forest Radar Measurements

ALBERT MONTEITH

Department of Space, Earth and Environment
Division of Microwave and Optical Remote Sensing
CHALMERS UNIVERSITY OF TECHNOLOGY

Göteborg, Sweden 2020

Temporal Characteristics of Boreal Forest Radar Measurements
ALBERT MONTEITH
ISBN 978-91-7905-344-4

Doktorsavhandlingar vid Chalmers tekniska högskola
Ny serie nr 4811
ISSN 0346-718X

Department of Space, Earth and Environment
Division of Microwave and Optical Remote Sensing
Chalmers University of Technology
SE-412 96 Göteborg
Sweden
Telephone: +46 (0)31-772 1000

Cover:
Photo of the tower-based radar used in this experiment.

Chalmers digitaltryck
Göteborg, Sweden 2020

Temporal Characteristics of Boreal Forest Radar Measurements
Thesis for the degree of Doctor of Philosophy
ALBERT MONTEITH
Department of Space, Earth and Environment
Division of Microwave and Optical Remote Sensing
Chalmers University of Technology

ABSTRACT

Radar observations of forests are sensitive to seasonal changes, meteorological variables and variations in soil and tree water content. These phenomena cause temporal variations in radar measurements, limiting the accuracy of tree height and biomass estimates using radar data. The temporal characteristics of radar measurements of forests, especially boreal forests, are not well understood. To fill this knowledge gap, a tower-based radar experiment was established for studying temporal variations in radar measurements of a boreal forest site in southern Sweden.

The work in this thesis involves the design and implementation of the experiment and the analysis of data acquired. The instrument allowed radar signatures from the forest to be monitored over timescales ranging from less than a second to years. A purpose-built, 50 m high tower was equipped with 30 antennas for tomographic imaging at microwave frequencies of P-band (420-450 MHz), L-band (1240-1375 MHz) and C-band (5250-5570 MHz) for multiple polarisation combinations. Parallel measurements using a 20-port vector network analyser resulted in significantly shorter measurement times and better tomographic image quality than previous tower-based radars. A new method was developed for suppressing mutual antenna coupling without affecting the range resolution. Algorithms were developed for compensating for phase errors using an array radar and for correcting for pixel-variant impulse responses in tomographic images.

Time series results showed large freeze/thaw backscatter variations due to freezing moisture in trees. P-band canopy backscatter variations of up to 10 dB occurred near instantaneously as the air temperature crossed 0°C, with ground backscatter responding over longer timescales. During nonfrozen conditions, the canopy backscatter was very stable with time. Evidence of backscatter variations due to tree water content were observed during hot summer periods only. A high vapour pressure deficit and strong winds increased the rate of transpiration fast enough to reduce the tree water content, which was visible as 0.5-2 dB backscatter drops during the day. Ground backscatter for cross-polarised observations increased during strong winds due to bending tree stems. Significant temporal decorrelation was only seen at P-band during freezing, thawing and strong winds. Suitable conditions for repeat-pass L-band interferometry were only seen during the summer. C-band temporal coherence was high over timescales of seconds and occasionally for several hours for night-time observations during the summer. Decorrelation coinciding with high transpiration rates was observed at L- and C-band, suggesting sensitivity to tree water dynamics.

The observations from this experiment are important for understanding, modelling and mitigating temporal variations in radar observables in forest parameter estimation algorithms. The results also are also useful in the design of spaceborne synthetic aperture radar missions with interferometric and tomographic capabilities. The results motivate the implementation of single-pass interferometric synthetic aperture radars for forest applications at P-, L- and C-band.

Keywords: Synthetic aperture radar, remote sensing, tomography, backscatter, temporal coherence, antenna array

ACKNOWLEDGEMENTS

The work in this thesis is the result of a unique experiment that I am fortunate to have been part of from its beginning, and with which I was entrusted with many of its responsibilities. I have my supervisor, Lars Ulander, to thank for this opportunity. I am fortunate to have had such a knowledgeable and supportive supervisor.

Thanks to Julia Kubanek, Tânia Casal, Klaus Scipal and Malcolm Davidson at ESA for all the positive feedback, encouragement and financial support during the past few years. It was a pleasure working with you. This work was also financially supported by the Swedish National Space Agency and the Hildur and Sven Wingquist Foundation for Forest Research.

For their guidance and great support in getting the project off the ground, I would like to thank Maciej Soja and Leif Eriksson. Thanks to Stefano Tebaldini and Susan Steele-Dunne for their guidance and interesting conversations regarding my work. I am also grateful for Martin Rönnfalk's help in making sense of the masses of data generated during this experiment. Thanks to my fellow PhD students and other colleagues at Chalmers, not only for helping me assemble the rodent-proof sensor cable system in the corridor, but also for contributing to a positive atmosphere and a great work environment.

Thanks to our colleagues at SLU for collecting forest inventory data, doing a terrestrial lidar scan at the experiment site, and, especially, Johan Fransson for proofreading this thesis and his endless enthusiasm. Thanks also to the team at FOI for installing several of the world's largest purpose-built trihedral corner reflectors at the experiment site, without which a calibration would not have been possible. Thanks also for acquiring airborne SAR measurements of the site.

A special thanks to Dr. Céline Heuzé for all the support, encouragement and fun times during the past few years.

Finally, I would like to thank my family, who have supported me all the way.

APPENDED PUBLICATIONS

This thesis is based on the work in the following appended publications:

I. L. M. H. Ulander, **A. R. Monteith**, M. J. Soja and L. E. B. Eriksson (2018). ”Multiport vector network analyzer radar for tomographic forest scattering measurements”. *IEEE Geoscience and Remote Sensing Letters*. Volume 15, issue 12, pp 1897 - 1901.

II. **A. R. Monteith** and L. M. H. Ulander (2018). ”Temporal survey of P- and L-band polarimetric backscatter in boreal forests”. *IEEE Journal of Selected Topics in Applied Earth Observations and Remote Sensing*. Volume 11, issue 10, pp 3564 - 3577.

III. **A. R. Monteith**, L. M. H. Ulander and S. Tebaldini (2019). ”Calibration of a ground-based array radar for tomographic imaging of natural media”. *Remote Sensing*. Volume 11, issue 24, pp 1 - 22.

IV. **A. R. Monteith** and L. M. H. Ulander (2020). ”Temporal characteristics of P-band tomographic radar backscatter of a boreal forest”. *Submitted manuscript.*

V. **A. R. Monteith** and L. M. H. Ulander (2020). ”Temporal coherence in a boreal forest at P-, L- and C-band: A tower-based radar study”. *Submitted manuscript.*

CONFERENCE PUBLICATIONS

The author has contributed to the following conference publications that are related to the work in this thesis, but are not appended to the thesis:

A. L. M. H. Ulander, M. J. Soja, **A. R. Monteith**, L. E. B. Eriksson, J. E. S. Fransson and H. J. Persson (2016). “BorealScat: A tower experiment for understanding temporal changes in P- and L-band backscattering from a boreal forest”. *Living Planet Symposium*, Prague, Czech Republic, 9-13 May 2016. European Space Agency, *(Special Publication)* ESA SP-740.

B. **A. R. Monteith**, M. J .Soja, L. M. H. Ulander and L. E. B. Eriksson (2016). “BorealScat: A tower-based tomographic and polarimetric radar experiment in the boreal forest at P-, L- and C-band”. *International Geoscience and Remote Sensing Symposium (IGARSS)*, Beijing, China, 10-15 July 2016, pp. 7458 - 7461.

C. L. M. H. Ulander and **A. R. Monteith** (2017). “Time series of P- and L-band forest backscatter from BorealScat”. *International Geoscience and Remote Sensing Symposium (IGARSS)*, Fort Worth, USA, 23-28 July 2017, pp. 4310 - 4313.

D. **A. R. Monteith** and L. M. H. Ulander (2018). ”Long-term P-band tomoSAR observations from the BorealScat tower experiment”. *International Geoscience and Remote Sensing Symposium (IGARSS)*, Valencia, Spain, 22-27 July 2018, pp. 8594 - 8597.

E. L. M. H. Ulander, **A. R. Monteith**, P.-O. Frölind, A. Gustavsson, A. Haglund, R. Ragnarsson and G. Stenström (2019). ”Airborne SAR for Calibration of P-Band Tower Radar”. *International Geoscience and Remote Sensing Symposium (IGARSS)*, Yokohama, Japan, 28 July-2 August 2019, pp. 541 - 544.

REPORTS

The author has contributed to the work presented in the following related reports which were delivered to, and approved by, the European Space Agency under ESA Contract No. 4000118576. The reports are available upon request from http://eopi.esa.int/Campaigns.

D**1.** L. M. H. Ulander, **A. R. Monteith** and M. J. Soja (2017). ”BorealScat Campaign Implementation Plan”, Deliverable D1. Contract No. ESA Contract No. 4000118576.

D**2.** L. M. H. Ulander and **A. R. Monteith** (2018). ”BorealScat Data Acquisition Report”, Deliverable D2. ESA Contract No. 4000118576.

D**3.** L. M. H. Ulander, **A. R. Monteith** and M. Rönnfalk (2018). ”BorealScat Final Report”, Deliverable D3. ESA Contract No. 4000118576.

D**4.** L. M. H. Ulander and **A. R. Monteith** (2019). ”BorealScat Campaign Implementation Plan”, Deliverable D4. ESA Contract No. 4000118576, contract change notice 1.

D**5.** L. M. H. Ulander and **A. R. Monteith** (2020). ”BorealScat Data Analysis Report”, Deliverable D5. ESA Contract No. 4000118576.

D**6.** L. M. H. Ulander and **A. R. Monteith** (2020). ”BorealScat Data Analysis Report”, Deliverable D6. ESA Contract No. 4000118576.

CONTENTS

Introduction

1

1.1 Motivation

Forests play a key role in the Earth's carbon cycle. CO_2 is emitted into the atmosphere through forest loss and is taken up by forests during growth. Together with fossil fuel emissions and uptake by the oceans, these are the main mechanisms forming the Earth's carbon budget. Quantifying the components of the carbon budget over time is necessary for understanding how natural sinks such as forests will respond to climate change, and to be able to define a permissible level of emissions for reaching a stable climate target. The largest uncertainties in the carbon budget are associated with the carbon emitted through land cover change and carbon uptake through forest growth, with uncertainties of 47% and 20% of their estimated values, respectively (Friedlingstein et al., 2019). These uncertainties are a result of the lack of measurement techniques for accurately quantifying the carbon content and CO_2 flux in forests on a global scale.

The dry biomass of forests consists of approximately 40-60% carbon (Thomas and Martin, 2012). This makes above-ground biomass change a proxy for the change in carbon stored on land. Radar observations have been shown to be sensitive to above-ground forest biomass. This has driven the development of new spaceborne radar sensors and the development of algorithms for estimating biomass using the acquired radar data. A variety of approaches are taken, from exploiting different properties of electromagnetic waves to observing forests using radar from multiple directions. The aim of these efforts is to extract structural information about forests to more accurately relate radar observables to above-ground forest biomass.

However, radar observables are not uniquely sensitive to biomass (Moghaddam, Durden, and Zebker, 1994). Changes in weather conditions and temporal variations in the water content of the soil and vegetation result in temporally varying radar observables. This may lead to large errors in biomass estimates (Saatchi and Moghaddam, 2000). It is not well understood how seasons, weather conditions and other natural phenomena affect radar measurements of forests, especially in boreal forests.

Boreal forests, found at latitudes of approximately 40°N to 70°N, make up the world's largest land biome. Boreal forests are responsible for 20% of the carbon absorbed by undisturbed forests (Pan et al., 2011). They also help regulate the climate through energy and water exchange, are the source of vast amounts of wood and provide habitats for animals in the developed world's last wilderness (Steffen et al., 2015). Of all forest biomes, boreal forests will experience the largest temperature increase during the 21st century (Gauthier et al., 2015). Thus, it is important to better understand how seasonal changes and weather variables influence radar observations of boreal forests. A better understanding of the temporal characteristics of boreal forest radar measurements will allow for the design of biomass estimation algorithms and spaceborne radar systems that are robust to temporal changes in radar observations.

1.2 This thesis

The work in this thesis aims to improve the understanding of how radar measurements of boreal forests change over time due to seasonal, meteorological and soil/tree moisture conditions. The knowledge gained will support the design of algorithms and spaceborne radar missions with the goal of estimating forest parameters such as biomass, stem volume and tree height. This knowledge will also reveal new forest radar remote sensing opportunities. The goals of the work described in this thesis were to

1. Design and implement a measurement system for acquiring time series of radar measurements in a boreal forest with similar electromagnetic wave properties and observation geometries to those of spaceborne radar systems.
2. Acquire radar measurement data over timescales of seconds to years, along with *in situ* data describing the meteorological and moisture conditions in the forest.
3. Analyse temporal variations in radar observables to explain their possible causes with regards to seasonal, meteorological and moisture conditions and separate the contributions of different forest structures.
4. Identify the implications of the observed variations on forest parameter estimation algorithms and the design of spaceborne radar missions.

Chapter 2 will follow with an introduction to radar remote sensing techniques, calibration and the effects of temporal variations. In Chapters 3 and 4, mechanisms by which temporal variations occur in forests are discussed from a physical perspective (electromagnetic scattering) and from a biological perspective (tree water relations), respectively. Chapter 5 introduces the experiment implemented in this thesis. Summaries of the appended papers are given in Chapter 6 before the conclusions in Chapter 7. A compilation of papers, which contain the main scientific outcomes of this thesis, are appended at the end.

Radar remote sensing of forests

2

The work in this thesis aims to support forest parameter estimation methods based on spaceborne synthetic aperture radar (SAR) data. The radar experiment implemented in this work is based on SAR imaging principles. Time series of similar observables as in SAR imaging were analysed. This chapter introduces radar remote sensing of forests from a SAR perspective.

2.1 Synthetic aperture radar

SAR is a radar remote sensing technique capable of producing high resolution images of large areas of the Earth's surface. Fine resolution imaging is necessary to resolve spatial inhomogeneities in forests and to separate forests from buildings, open fields and water bodies. A fine resolution is also necessary for reducing the variance of radar observables. Imaging over large areas is necessary for global coverage. A SAR consists of a radar system mounted on a movable platform such as an aircraft or spacecraft. Multiple pulses are transmitted from the platform as it moves in space, which then reflect off the Earth's surface and are received again by the radar. The received pulses are combined through signal processing algorithms to produce an image of the surface reflectivity.

Spaceborne SARs are typically mounted on satellites in low Earth orbit, allowing large areas of the Earth's surface to be repeatedly imaged at intervals of days to months. A significant advantage that SAR has over other Earth observation techniques (e.g. lidar and hyperspectral imaging) is that the electromagnetic waves, with frequencies below 20 GHz, are capable of penetrating the atmosphere even in the presence of clouds. Observations through clouds are important since the two largest forest biomes, tropical and boreal, are often covered by clouds. Being an active remote sensing technique, SAR images can be acquired during both day and night.

The maps of surface reflectivity resulting from SAR measurements can be converted into maps of forest parameters such as biomass (Wu, 1987; Le Toan et al., 1992; Hussin, Reich, and Hoffer, 1991; Dobson et al., 1992; Ranson and Guoqing, 1994). Accurate biomass estimation starts with the design of the radar instrument, the selection of electromagnetic wave properties and the orbital pattern of the satellite.

2.2 Backscatter

The power echoed from an object can be related to the object's radar cross-section σ through the radar equation. For a monostatic radar with atmospheric and internal losses neglected, the radar equation is

$$P_r = P_t \frac{G^2 \lambda^2}{(4\pi)^3 R^4} \sigma, \tag{2.1}$$

where P_r is the received power, P_t is the transmitted power, G is the antenna gain, λ is the wavelength and R is the radar-object distance. Forests consist of many complicated structures resulting in randomly distributed scatterers. For two-dimensional SAR images it is useful to define the *backscattering coefficient*

$$\sigma^0 = \frac{\langle \sigma \rangle}{A}, \tag{2.2}$$

which is the average radar cross-section per unit area A. The backscattering coefficient is a property of a surface element describing the magnitude of power scattered back towards the radar relative to the power emitted by the radar. Larger trees, or a higher tree density per unit area, will scatter a larger fraction of the incident power back towards the radar, resulting in a higher σ^0. Many forest parameter estimation algorithms are based on relating σ^0, as measured by a SAR, to the forest parameter of interest.

Frequency bands

The σ^0 of a forest depends on both the radar parameters and the observed forest scene. Radar parameters that affect backscatter are the frequency and polarization of the electromagnetic waves, the aspect angle and the angle between the wave direction and ground surface normal, called the *incidence angle*. The choice of radar frequency determines which structures within the forest will contribute to the backscatter. High radar frequencies such as X-band (8-12 GHz) and C-band (4-8 GHz) are scattered by small structures in the upper canopies of forests. At lower frequencies, such as L-band (1-2 GHz), electromagnetic waves are capable of penetrating the forest canopy and scatter off larger structures such as branches and trunks, which contain the majority of a tree's biomass. Lower frequency SARs are, thus, better suited for biomass estimation when using SAR backscatter. Better sensitivity to high biomass values can be obtained with a SAR operating at P-band (420-450 MHz) (IEEE, 2003; Israelsson, Askne, and Sylvander, 1994). Electromagnetic waves with even lower frequencies (30-300 MHz) provide the best backscatter sensitivity to forest biomass (Israelsson et al., 1997; Fransson, Walter, and Ulander, 2000; Smith and Ulander, 2000; Smith-Jonforsen, Ulander, and Luo, 2005), but waves at such low frequencies are distorted by the ionosphere, limiting their use to airborne SARs (Shteinshleiger et al., 1997). A usually undesired consequence of the greater canopy penetration in low frequency SAR imaging (L- and P-band) is that the ground can contribute significantly to the backscatter (Alemohammad et al., 2019). Ground conditions such as slope, roughness and moisture content can have a significant effect on backscatter (Banda et al., 2020).

Polarimetry

The polarisation of an electromagnetic wave specifies the directional characteristics of electric field oscillations. A fully polarimetric radar is capable of transmitting and receiving both horizontally (H, parallel to the Earth's surface) and vertically (V, orthogonal to H and the direction of propagation) polarised waves. The scattered fields in each pixel of a SAR image can then be separated into the HH, HV, VH and VV contribution, where the first letter is the receiving polarisation and the second the transmitted polarisation (Ulaby et al., 2014; Lee and Pottier, 2009). The opposite of this convention is also seen in literature. The rationale behind SAR polarimetry is that different polarisations result from different electromagnetic scattering mechanisms, allowing a decomposition of scattering contributions from different structures in a forest. Different polarisations thus have different degrees of sensitivity to biomass. In boreal forests, HV and HH backscatter have been found to show the greatest sensitivity to biomass at P- and L-band. Several P-band biomass estimation models include a combination of backscatter terms from different polarisations (Soja, Sandberg, and Ulander, 2013; Villard and Le Toan, 2015; Truong-Loï, Saatchi, and Jaruwatanadilok, 2015).

Speckle

A resolution cell size for an imaging radar system is typically on the order of 1 to 100 m. Such a forest region contains many scattering elements (e.g. leaves, twigs, branches, stems, undergrowth and ground). Depending on their locations and scattering strength, the electromagnetic fields scattered from these structures may add up constructively or destructively in any given direction. As a result, the backscatter varies significantly from pixel to pixel in a SAR image, a phenomenon known as *speckle*. Little knowledge about a forest's properties can be inferred from the backscatter value of a single pixel in a SAR image. Backscatter can only be reproducibly connected to forest properties when considering the moments of several independent samples, also called *looks*. Independent samples can be obtained from multiple antenna beams, multiple frequency bands or, most commonly, from multiple resolution cells in a SAR image. An unbiased estimate of the backscatter is produced by the sample average

$$\hat{\sigma}^0 = \frac{1}{L}\sum_{i=1}^{L}\sigma_i^0, \tag{2.3}$$

where σ_i^0 is the i^{th} backscatter sample. The variance of this estimate depends on the true backscatter σ^0 and the number of looks L according to (Lee and Pottier, 2009)

$$\text{Var}[\hat{\sigma}^0] = \frac{(\sigma^0)^2}{L}. \tag{2.4}$$

This can be seen in Figure 2.1, where the distribution for the backscatter estimate becomes narrower and more centred around the true value for a higher number of looks.

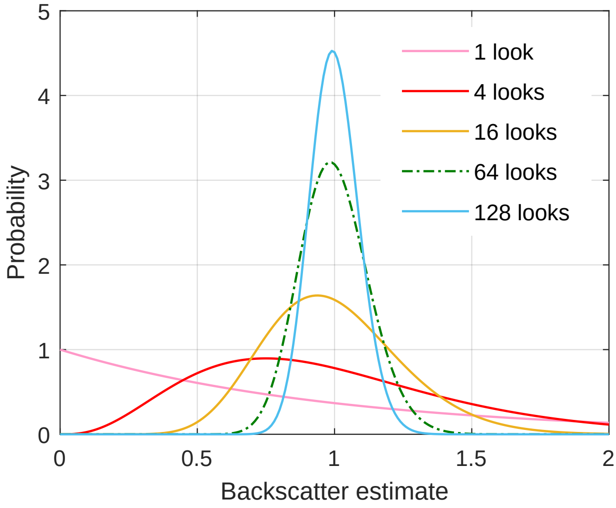

Figure 2.1. *Probability density function of the backscatter estimate* $\hat{\sigma}^0$ *for different numbers of looks when* $\sigma^0 = 1$*. The single look probability density function is a negative exponential function (Lee and Pottier, 2009). The probability density functions for multilooked backscatter estimates are described by Chi-square distributions with degrees of freedom equal to twice the number of looks.*

2.3 Interferometry

SAR interferometry provides information about the effective scattering height (Bamler and Hartl, 1998). Larger trees with more biomass tend to have a higher scattering height, providing a SAR observable that is related to biomass and can be included in estimation models. An alternative use of interferometry is to cancel out a scattering contribution such as the ground (d'Alessandro et al., 2020). SAR interferometry makes use of two SAR images over the same forest site, where the antenna platform views the forest from slightly different angles for the two images (Moreira et al., 2013). The two co-registered images are combined to produce two commonly used observables: the interferometric coherence γ and the interferometric phase $\Delta\phi$.

Temporal decorrelation

The interferometric phase is directly related to the effective scattering height, but has a large variance if the interferometric coherence between the two images is low. The coherence describes the extent of phase noise and takes a value from 0 (completely random phase) to 1 (deterministic phase). The coherence is both a measure of quality of interferometric phase measurements and a source of information about the forest scene. The coherence can be expressed as a product of four coherence contributions (Zebker and Villasenor, 1992; Ulaby et al., 2014)

$$\gamma = \gamma_{SNR} \cdot \gamma_{system} \cdot \gamma_{spatial} \cdot \gamma_{temporal}. \tag{2.5}$$

γ_{SNR} is the decorrelation due to thermal noise and depends on the signal-to-noise ratio (SNR). System decorrelation γ_{system} is caused by imperfections in the radar sensor and processing scheme. Spatial decorrelation $\gamma_{spatial}$ results from viewing the scene from different angles in the two SAR images. Temporal decorrelation $\gamma_{temporal}$ is an unwanted phenomenon whereby the scattering properties of the forest change between the two SAR acquisitions, resulting in poor scattering height estimates (Hagberg, Ulander, and Askne, 1995; Askne et al., 1997; Cloude and Papathanassiou, 1998; Santoro and Cartus, 2018). Temporal decorrelation depends on the amount of scattering changes as well as the SAR frequency. Small forest structures such as twigs and leaves, which scatter high frequency electromagnetic waves (e.g. C- and X-band) more easily, are less stable in time. The higher the SAR frequency, the greater the temporal decorrelation between two interferometric SAR acquisitions. Temporal decorrelation has been observed to be caused by wind, rain, soil moisture changes, snow, freeze/thaw changes, vegetation growth and changes in tree water content (Koskinen et al., 2001; Eriksson et al., 2003; Pulliainen, Engdahl, and Hallikainen, 2003; Lee et al., 2013). Temporal decorrelation is also more likely to occur for longer time intervals between the two acquisitions. This interval is called the *temporal baseline*, and is determined by the orbit of the SAR satellite.

Temporal baselines

SAR interferometry can be achieved by multiple orbital passes of a SAR satellite over the same site, known as *repeat-pass* SAR interferometry. A drawback of this method is that the orbital passes are separated by temporal baselines of hours to days, during which moisture and geometrical changes can take place in the forest, resulting in severe temporal decorrelation at frequencies of L-band and higher. This problem can be overcome by having two antennas on the same platform (e.g. NASA's Shuttle Radar Topography Mission) or two antenna platforms orbiting the Earth in close proximity (e.g. DLR's TanDEM-X mission), called *single-pass* interferometers. In the latter case, the acquisition time interval between the two SAR images may still be on the order of milliseconds to seconds, during which significant temporal decorrelation could occur in forests due to wind (Narayanan, Doerr, and Rundquist, 1992; Billingsley, 2002).

Coherence estimation

The complex correlation coefficient between L samples (pixels) from two SAR images s_1 and s_2, with their phases corrected for topographic phase variations, is

$$\widehat{\gamma} = |\widehat{\gamma}| e^{j\widehat{\Delta\phi}} = \frac{\sum_{i=1}^{L} s_1^i \cdot s_2^{i*}}{\sqrt{\sum_{i=1}^{L} \left|s_1^i\right|^2 \sum_{i=1}^{L} \left|s_2^i\right|^2}}, \tag{2.6}$$

where $|\widehat{\gamma}|$ is the estimated coherence magnitude, or simply *coherence*, and $\widehat{\Delta\phi}$ is the estimated interferometric phase resulting from L looks. As with backscatter estimates, the variance of $|\widehat{\gamma}|$ decreases as the number of looks increase. The estimate $|\widehat{\gamma}|$ is also biased, with a lower bias as the number of looks increases. Both the bias and variance of coherence estimates are dependent on the true coherence as shown in Figure 2.2.

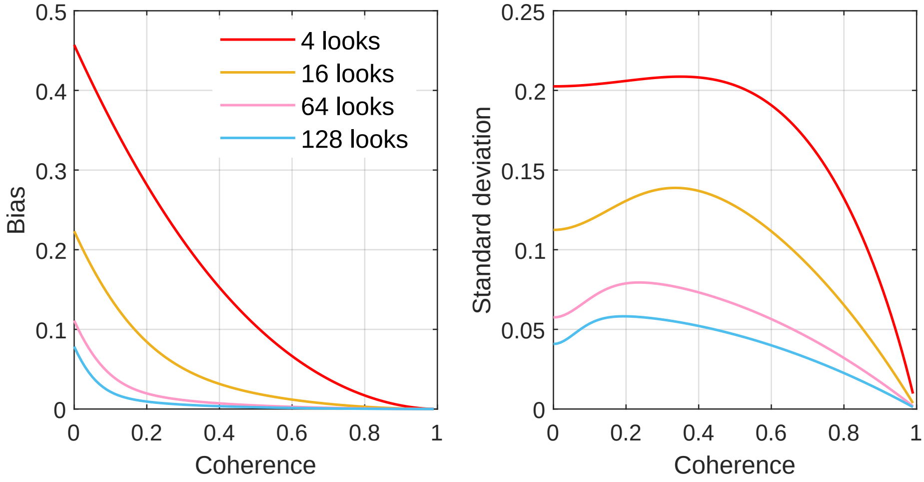

Figure 2.2. *Bias and standard deviations of coherence estimates for different numbers of looks and as a function of the true coherence (Touzi et al., 1999).*

2.4 Tomography

SAR tomography allows the separation of scatterers with different heights (Reigber and Moreira, 2000). This is useful for separating the backscatter contributions from the forest canopy and the ground, providing observables that are more closely related to above-ground biomass (Tebaldini and Rocca, 2012; Minh et al., 2016). This is achieved by coherently combining multiple SAR images of the same forest site, each acquired at a different incidence angle. The result is a three-dimensional volume of the forest reflectivity. Tomography can be viewed as an extension to interferometry, where the scene is viewed from a 2D synthetic aperture (Homer, Longstaff, and Callaghan, 1996). While interferometry reveals information about the effective scattering height of a forest, tomography reveals information about the 3D structure of the forest. This requires penetration of the electromagnetic waves into the canopy, making low frequency SARs such as P- and L-band more favourable options for implementing tomography (Tebaldini and Rocca, 2012).

Revisit times

Several orbital passes of the SAR satellite are required to form a SAR tomogram. This technique is called *repeat-pass* SAR tomography. The more orbital passes, the better the reconstruction of the scene's reflectivity. The vertical resolution is determined by the vertical aperture, while the spatial separation between orbital passes determines the height at which ambiguities appear. The temporal baselines between these acquisitions may result in severe temporal decorrelation, reducing the quality of tomography observables. Repeat-pass SAR tomography of forests is, therefore, only feasible at lower frequencies, such as at P-band or lower, where larger changes in geometry or dielectric properties of the forest are necessary to result in significant temporal decorrelation (Minh et al., 2015).

Due to its ability to penetrate forest canopies, there is also an interest in SAR tomography at

L-band, although the severity of temporal decorrelation at L-band does not facilitate repeat-pass SAR tomography of forests. Instead, the aim is to acquire an interferometric pair of SAR images at the same time using two antenna platforms orbiting in close formation, i.e. a single-pass interferometer, such that temporal decorrelation is negligible. Several such interferometric pairs acquired with a single-pass interferometer over multiple orbital passes are then combined to form a SAR tomogram that is more robust to temporal decorrelation (Tebaldini and Ferro-Famil, 2017). This technique is called *correlation tomography*.

Tomographic image reconstruction

Image reconstruction from the measurement of scattered fields is an inherently ill-posed problem (Pastorino, 2010). Different approaches have been taken for reconstructing tomographic data from measurements across the 2D synthetic aperture. The geometry of spaceborne and most airborne tomographic SAR observations allows the image reconstruction problem to be reduced to a spectral estimation problem. Both model-based and model-free spectral estimation methods have been used for tomographic reconstruction. Model-based spectral estimation methods require a number of parameters describing the statistics of the received signal, scene geometry or scattering mechanisms (Cloude, 2006; Zhu and Bamler, 2010; Pardini et al., 2012a). Describing the variety of species, scattering differences at different frequencies and moisture effects makes model-free spectral estimation the preferred alternative for tomographic imaging of forests (Aghababaei et al., 2020). Model-free approaches include Fourier beamforming and Capon spectral estimation. Capon spectral estimation results in better resolution, resolving fine structural details (Hajnsek et al., 2008). Beamforming is the preferred alternative when radiometric accuracy is the priority (Aghababaei et al., 2020). In addition to worse resolution, beamforming results in stronger sidelobes.

Spectral estimation methods are only applicable when the vertical extent of the scene is small compared to the distance between the radar and the scene. For certain airborne tomographic SAR geometries, and especially ground-based tomography systems, this assumption does not hold because lines of constant phase curve within the forest canopy. For maximum tomographic image reconstruction quality, backprojection methods must be used in such cases (Frey and Meier, 2011). Backprojection algorithms easily accommodate uneven spatial baselines and different propagation velocities within natural media such as snow (Tebaldini et al., 2016). In a backprojection, the value of each voxel is the coherent sum of observations from different angles, each compensated for signal delays between antenna and voxel positions.

2.5 Calibration

The magnitude or phase of a SAR image pixel is associated with a certain frequency, polarisation and incidence angle. While the dimensionality of SAR data provides a great amount of information about the observed scene, it introduces significant calibration challenges for mission designers, operators and users of SAR data.

Radiometric calibration

Calibration of the magnitude of a SAR image is necessary for relating the measured backscatter to a geophysical variable such as biomass regardless of the SAR sensor used, acquisition time or geographical location (Oliver and Quegan, 2004). A common calibration method is to place reflectors with known scattering properties in the observed scene (Ulander, 1991). Metal trihedral corner reflectors strongly reflect electromagnetic waves with little sensitivity to the direction of the radar relative to the reflector. The polarisation of an electromagnetic wave reflected by a trihedral corner reflector is the same as that of the incident wave. Cross-polarised waves (HV and VH) are not reflected. Calibration of cross-polarised radar channels can instead be done using dihedral corner reflectors, but the scattering characteristics are sensitive to their orientation relative to the radar. The use of reference reflectors assumes that reflections from the surrounding objects are much smaller than that of the reflector (Ulaby et al., 2014). These reflectors are often placed on open, flat terrain which does not have a large σ^0.

Phase calibration

When coherently combining SAR images, it is important that the phases of SAR images are calibrated relative to one another. Phase errors are especially common in SAR tomography, causing sidelobes and defocusing (Tebaldini and Monti Guarnieri, 2010). The errors arise from uncertainties in propagation delays and positions of the antenna phase centres. To avoid such problems, the effective positions of antenna phase centres need to be known to within a fraction of the radar's wavelength. Phase calibration is the process by which these errors are estimated and compensated for, resulting in focused tomograms. A reference reflector such as a trihedral corner reflector or transponder can be used for calibrating phases. However, the acquisition geometry of a SAR satellite orbiting the Earth constantly changes, requiring different calibration constants for each combination of SAR images. Since it is not feasible to place reference reflectors all over the globe, other features in the scene must be used for phase calibration. Stable targets can be detected in the scene and used for calibration (Tebaldini and Monti Guarnieri, 2010), but the presence of such targets cannot be guaranteed. Phase calibration has been achieved by using polarimetric decompositions to isolate the scattering contribution of the ground (Tebaldini, 2009), although the ground topography must be known. Phases can be calibrated through iterative minimisation of the tomographic image entropy (Pardini et al., 2012b), but this approach comes with a large computational load. A method for tomographic phase calibration has also been developed based on jointly estimating antenna phase centres and equivalent target phase centres with a single polarisation (Tebaldini et al., 2015). Tomographic phase calibration is an active research topic.

2.6 Current and future spaceborne SARs

The lowest-frequency civilian SARs currently in Earth's orbit are JAXA's ALOS-2 satellite and SAOCOM-1A from CONAE (Argentina). The PALSAR-2 SAR on ALOS-2 is quad-polarised (HH, HV, VH and VV). However, few observations per year and JAXA's data policy limits the use of PALSAR-2 data on a global scale. Due to the sensitivity of L-band radar signatures to temporal variations in forests, these missions are not optimal for SAR interferometry or SAR tomography over forests. A possible future mission, Tandem-L by DLR, will feature two SARs flying in formation such that an interferometric pair can be acquired within a time interval on the order of seconds, allowing for SAR interferometry and SAR correlation tomography of forests (Moreira et al., 2015). An upcoming mission by ESA, ROSE-L, is planned to feature at least two L-band SARs (Davidson et al., 2018). The exact number of satellites and their orbital configuration are yet to be determined, but it is likely that temporal baselines may be suitable for interferometric and tomographic SAR imaging of forests. Another L-band SAR, planned for launch in 2022, is NISAR by NASA and ISRO (India). NISAR will also feature an S-band (2 to 4 GHz) SAR. The revisit time of NISAR will be 12 days,

Forest monitoring at C-band is also of high interest, which is driven by the freely-available SAR data from ESA's Sentinel-1 satellites (Torres et al., 2012; Torres et al., 2017). This dual-polarised SAR mission currently consists of two identical satellites (Sentinel-1A and 1B) in Earth's orbit but 180° out of phase, offering a 6-day repeat cycle. The high temporal decorrelation over this timescale at C-band does not facilitate interferometry and tomography over forests using Sentinel-1 data. A proposed mission concept is to add a companion satellite to one of the existing Sentinel-1 satellites to allow the acquisition of interferometric pairs with little temporal decorrelation (Regan, Silvestrin, and Fernandez, 2016; Sephton and Wishart, 2013; Rott et al., 2017), including a candidate mission for ESA's Earth Explorer 10 (López-Dekker et al., 2019). A unique C-band SAR is the Earth Explorer 10 candidate mission Hydroterra (Hobbs et al., 2018). This SAR will be placed in a geosynchronous orbit with nearly half the world within view at all times. The major advantage of this concept is that images can be produced at intervals of hours, capturing scattering dynamics during the day, such as soil moisture variations. However, coherent integration times for image formation are on the order of minutes to hours, over which wind is likely to disturb forest canopies.

One tandem mission is already in orbit, DLR's TanDEM-X mission, consisting of two quad-polarised X-band SAR sensors orbiting in close formation (Krieger et al., 2007). The interferometric pairs acquired during tight formation flying over forests have essentially no temporal decorrelation. These SAR observables have been shown to be useful for estimating forest biomass in boreal forests assuming a known digital terrain model and suitable allometric equations (Askne et al., 2013; Soja, Persson, and Ulander, 2015; Askne, Soja, and Ulander, 2017).

With regards to radar remote sensing of forests, a SAR operating at a frequency capable of better forest volume penetration than L-band is needed. This will allow for better backscatter sensitivity at higher values of forest biomass and better illumination of the forest volume for SAR tomography. This need will be fulfilled by ESA's BIOMASS mission which was selected to be ESA's 7th Earth Explorer in 2013 (ESA, 2012; Quegan et al., 2019). This single satellite will feature a quad-polarised SAR and will be the first spaceborne P-band SAR. The satellite will operate in a repeat-pass SAR tomography mode for the first nine months, providing vertical distributions of forest backscatter. Tomograms will be reconstructed from seven acquisitions, each separated by three days. High temporal coherence on the order of days to months is, therefore, desirable at P-band. The launch for BIOMASS is planned for the year 2022.

2.7 Studying temporal variations

Radar platforms for temporal studies

Temporal variations in scattering characteristics can affect radar remote sensing observations at timescales ranging from less than a second to years. Studying these variations requires a radar capable of making frequent observations (fine temporal resolution) for a long period of time (long temporal coverage). While the mission lifetime of low Earth orbiting SARs is several years, the revisit time over forested regions of the globe is usually a few days, weeks or months. Temporal variations due to wind, transpiration and freeze/thaw cycles cannot be resolved with such instruments. Most low Earth orbiting SARs are also in a sun-synchronous orbit, whereby the forest is observed during only two times of the day: dawn and dusk. Diurnal dynamics can be reconstructed with different low Earth orbits, such as that of the International Space Station (ISS). Diurnal scattering patterns could be reconstructed from data acquired by the RapidScat radar mounted on the ISS, but only at a single observation per day over a period of two months (van Emmerik et al., 2017). SARs in a geostationary or geosynchronous orbit are theoretically capable of making observations at hourly intervals, albeit at a lower spatial coverage than low Earth orbiting SARs (Hobbs et al., 2018).

The study of temporal variations in SAR observables, in particular temporal decorrelation, was a goal of several airborne SAR campaigns (Hajnsek et al., 2008; Lavalle, Simard, and Hensley, 2012; Lee et al., 2013). While allowing greater control over observation times and geometries, airborne SARs have observation intervals on the order of minutes to hours, but are too expensive to run for more than a few hours at a time. Airborne SAR data are, thus, temporally sparse. Observations over timescales of minutes down to less than a second can be carried out over longer periods using radars that are fixed on the ground. Ground-based observations are less expensive than airborne and spaceborne systems, but their spatial coverage is much smaller, typically being on the plot scale. In most ground-based radar experiments, the radar has been mounted on a portable tower, scissor lift, cherry picker or other mobile elevating work platform (Ulaby, 1975; Ulaby and Wilson, 1985; De Loor, Hoogeboom, and Attema, 1982; O'Neill et al., 2006; Morrison, Bennett, and Solberg, 2013; Nagarajan et al., 2014). Such portable systems are limited in the size of the antenna construction and their stability in strong winds, making them less suitable for year-round monitoring using array-based radars. Their portability also makes their users more inclined to observe multiple sites instead of gathering multi-year time series. To overcome these limitations, a radar can be mounted on a fixed tower. Figure 2.3 illustrates the relationship between the temporal resolution, temporal coverage and spatial coverage of platforms for radar imaging.

Tower-based imaging radars

The more stable construction of towers limits their sway in the wind, allowing observations from larger heights. Observations from larger heights increases the spatial coverage to the stand scale. Towers are also better suited for mounting multi-antenna radar systems in a stable manner. In order to study the temporal variation of SAR observables in tropical forests, the TropiScat campaign was initiated in French Guiana (Albinet et al., 2012). The experiment consisted of a 55 m high tower equipped with an antenna array capable of acquiring quad-polarimetric radar data over a tropical

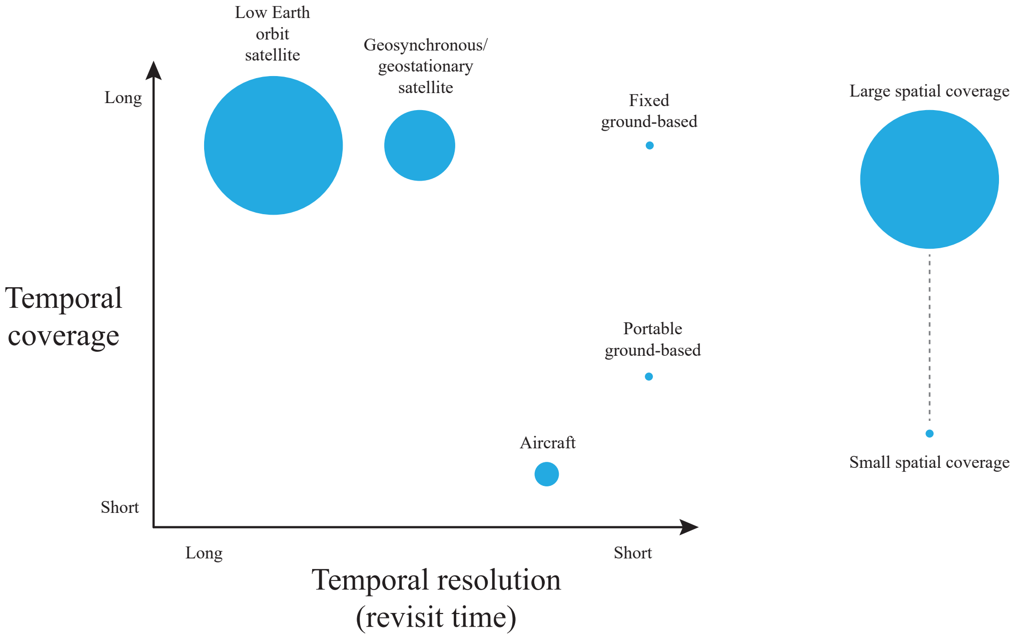

Figure 2.3. *Relationship between the temporal resolution, temporal coverage and spatial coverage of platforms for radar imaging.*

forest site at P- and L-band[1]. The antenna array allowed tomographic analyses of the forest site over time (Minh et al., 2013). Data were acquired at intervals of 15 minutes for more than a year. Data from on-site meteorological and soil moisture sensors allowed an analysis of how SAR observables are affected by environmental variations in tropical forests. This experiment provided valuable information about the temporal coherence at different timescales, diurnal variations in backscatter, changes in the effective scattering height with time and what scattering mechanisms are involved. It also provided the optimal times of the day (6:00 and 18:00) for acquisitions by the future BIOMASS satellite such that the effects of environmental parameters on SAR observables are minimised (Borderies et al., 2013). In 2015, this study was extended with a second tower-based radar, AfriScat, in the tropical forests of Ghana (Albinet et al., 2015). A similar, but smaller-scale experiment where a single temperate tree in France was studied showed that the backscatter and temporal coherence was very sensitive to temperature and moisture conditions (Albinet et al., 2016). This suggested dependence of SAR observables on the dielectric constant of the soil and tree trunk, as well as transpiration mechanisms. In 2018, the TropiScat radar was extended to include C-band observations, albeit without tomographic capabilities, with a focus on temporal decorrelation (El Idrissi Essebtey et al., 2020). Together with measurements of evapotranspiration from the flux tower on which the radar is mounted, C-band temporal coherence was shown to be sensitive to the diurnal transpiration cycles of the forest.

---

[1] L-band was defined as 800-1000 MHz, which is lower than the IEEE definition (1000-2000 MHz).

The knowledge gap

The results from these experiments cannot be extrapolated to boreal forests due to significant differences in climate and forest structure between the two biomes. No experiment studying the temporal variation of SAR observables over timescales of minutes to years has been done before in boreal forests. To fill this knowledge gap, the BorealScat tower-based radar campaign was initiated in Remningstorp, Sweden by Chalmers University of Technology in co-operation with the Swedish University of Agricultural Sciences (Ulander et al., 2016). The BorealScat experiment is the main topic of this thesis and is introduced in Chapter 5. Observations by the Finnish Meteorological Institute are also underway in Sodankylä, Finland using a new tower-based SAR called SodSAR (Luojus et al., 2020).

Microwave scattering in forests

3

To understand how radar measurements of a forest can vary with time, we need to understand what properties of the observed scene cause the reflections measured by a radar. This chapter provides an introduction to macroscopic electromagnetic scattering in forests at microwave frequencies.

3.1 The scattered field

Currents in the transmitting radar antenna produce an electromagnetic wave with electric field $\boldsymbol{E}^i(\boldsymbol{r})$ (where $\boldsymbol{r}$ is a point in space) that propagates through the Earth's atmosphere and encounters objects in the observed scene. Currents are induced in the scene, producing a scattered electromagnetic field with electric field $\boldsymbol{E}^s(\boldsymbol{r})$ which is sensed by the radar's receiving antenna. While $\boldsymbol{E}^i(\boldsymbol{r})$ is entirely controlled by system parameters, such as frequency, output power and antenna pattern, $\boldsymbol{E}^s(\boldsymbol{r})$ is affected by unknown structural and material properties of the observed scene. In the time-harmonic case, the scattered field at location $\boldsymbol{r}$ is (Solimini, 2016; Kristensson, 2016)

$$\boldsymbol{E}^s(\boldsymbol{r}) = j\omega \left[\mathbf{I} + \frac{1}{k^2}\nabla\nabla\right] \cdot \iiint_{V'} \frac{e^{-jk|\boldsymbol{r}-\boldsymbol{r'}|}}{4\pi\left|\boldsymbol{r}-\boldsymbol{r'}\right|}\boldsymbol{J}(\boldsymbol{r'})dV', \tag{3.1}$$

where $j = \sqrt{-1}$, ω is the angular frequency of the radar, $\mathbf{I}$ is the unit dyadic in three dimensions[1], k is the spatial wavenumber of a vacuum, $\boldsymbol{r'}$ is a spatial coordinate within the scattering volume V' and $\boldsymbol{J}(\boldsymbol{r'})$ is the induced current density within V'. The scattered field in (3.1) is a summation of fields contributed to by many elemental current densities distributed throughout the volume V' containing the scene illuminated by the radar (see Figure 3.1). The complex exponential term, in combination with the summation over the volume, results in constructive or destructive interference between these scattering contributions. Structures that are large and have smooth surfaces relative to the wavelength, such as tree trunks and smooth topographies, result in coherently adding fields (*coherent scattering*). This gives rise to strong specular reflections off straight stems and smooth ground surfaces. For scatterers with a random structure, such as tree canopies containing many small scatterers, the scattering contributions may add up in phase or out of phase in any direction. This produces speckle in radar images, which was described in the previous chapter. The denominator $|\boldsymbol{r} - \boldsymbol{r'}|$ models free space loss.

The strength of each scattering contribution depends on the apparent current density[2] (Solimini, 2016)

$$\boldsymbol{J}(\boldsymbol{r'}) = j\omega\left[\epsilon(\boldsymbol{r'}) - \epsilon_0\right]\boldsymbol{E}(\boldsymbol{r'}), \tag{3.2}$$

---

[1] For any vector $\mathbf{a}$, $\mathbf{I} \cdot \mathbf{a} = \mathbf{a}$.

[2] Equation 3.2 assumes an isotropic material with magnetic permeability equal to that of a vacuum. Most natural media have a magnetic permeability equal to that of a vacuum, but not all are isotropic.

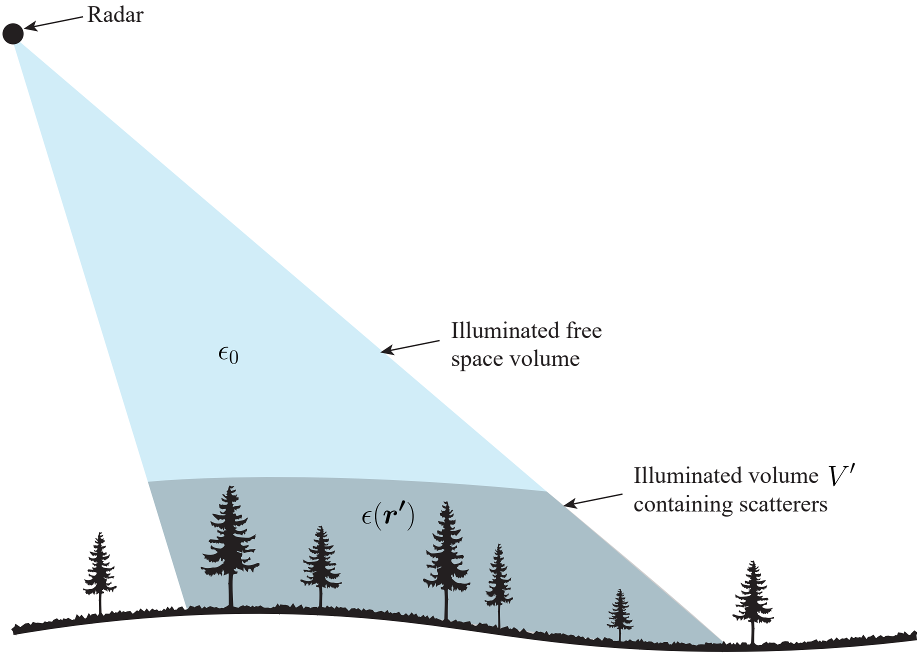

Figure 3.1. *The electromagnetic wave generated by the radar is scattered in multiple directions by objects within the volume* V' *with electric permittivity* $\epsilon(\boldsymbol{r'})$.

where $\epsilon(\boldsymbol{r'})$ is the complex electric permittivity of the material and ϵ_0 is the electric permittivity of a vacuum. The total electric field $\boldsymbol{E}(\boldsymbol{r'})$ is the sum of the incident field $\boldsymbol{E}^i(\boldsymbol{r'})$ and the scattered field $\boldsymbol{E}^s(\boldsymbol{r'})$. The current density in a volume element in the scene is, therefore, dependent on both the incident field produced by the radar and the fields scattered by all other volume elements in the scene. This causes electromagnetic couplings between volume elements in the scene, resulting in, for example, multiple scattering mechanisms between the ground, stems and canopies. The factor $\epsilon(\boldsymbol{r'}) - \epsilon_0$ in (3.2) shows that the larger the electric permittivity of the material relative to that of the surrounding free space, the stronger the induced current density. Any temporal variation in measurements by a stationary radar must be due to variations in either the value or the spatial distribution of $\epsilon(\boldsymbol{r'})$.

3.2 Dielectric properties of forest materials

The permittivity ϵ of a natural material, such as soil or living wood, characterises how charges in the material respond to forces caused by electromagnetic fields. The change in spatial distribution of charges, in the presence of an externally applied electromagnetic field, gives rise to a new electromagnetic field. This is the source of the scattered field sensed by the radar. Several atomic and molecular mechanisms can result in a change in the spatial distribution of charges (Raicu and Feldman, 2015). In natural materials, for frequencies up to approximately 100 GHz, the dominant mechanisms contributing to ϵ are ionic conduction and the rotation of water molecules.

Due to their permanent electric dipole moments, water molecules experience a torque in an electric field, forcing molecules to align with the electric field direction. This alignment is disturbed by collisions with other thermally agitated molecules and hydrogen bonds that form and break over time (Raicu and Feldman, 2015). Temperature plays a key role in these molecular dynamics, making the permittivity dependent on temperature. Water molecules are capable of following changes in an electromagnetic field up to approximately 5 GHz, beyond which alignment with the field becomes resisted by the rotational inertia of the molecules. The permittivity is further affected by the presence of ions, the volumetric water content in the material and the supporting structure. Forest materials such as soil and wood are inhomogeneous mixtures of solid material, air and water. The wavelengths of Earth observation radars are typically larger than the size of these inhomogeneities and, thus, only the effective permittivity of the bulk material is considered. The permittivity of forest materials can be explained using dielectric mixture models, taking into account the permittivity of the material's constituents and their respective volume fractions (Sihvola, 1999).

An isotropic dielectric material's response to an alternating electromagnetic field is described by the complex permittivity

$$\epsilon = \epsilon_0[\epsilon' - j\epsilon'']. \tag{3.3}$$

Since ϵ_0 is known, the quantity of main interest is $\epsilon' - j\epsilon''$, called the *relative permittivity*. The real part ϵ' (traditionally called the *dielectric constant*) accounts for the extent to which water molecules orientate along the direction of the electric field. The strength of the scattered field relative to the strength of the incident field is, therefore, primarily determined by ϵ'. The imaginary part ϵ'' (called the *dielectric loss factor*) accounts for electromagnetic energy dissipated in the material. Energy is dissipated through collisions between water molecules as they rotate in an oscillating electromagnetic field. If ions are present, energy is also lost through Ohmic conduction in the material. The angle $\tan^{-1}(\epsilon''/\epsilon')$, is the phase difference between the total electric field and current density. Changes in ϵ' and ϵ'' can cause a change in both the magnitude and phase of the scattered field. Both the radar backscatter and temporal coherence are, therefore, affected by temporal variations in ϵ' and ϵ''.

Permittivity of water and ice

The permittivity of natural materials such as soil and living wood is dominated by that of water (Salas et al., 1994). As shown in Figure 3.2, ϵ' and ϵ'' of liquid water vary with frequency and have a moderate temperature dependence. In ice, the rotation of water molecules is severely limited, resulting in a significantly lower ϵ'. This results in a major drop in radar backscatter as the temperature drops below 0°C. The largest backscatter variations observed in this thesis were due to air temperature variations past 0°C. For ice, ϵ' has a negligible temperature dependence and is constant with frequency up to 300 GHz (Mätzler and Wegmüller, 1987). Ice also has $\epsilon'' \approx 0$, which results in negligible attenuation of waves in frozen materials. This property allows tomographic imaging of glaciers down to tens of metres (Tebaldini et al., 2016).

For water with large amounts of dissolved ions (saline water), the permittivity is mainly affected in the form of a significant increase in ϵ'' at low frequencies (<1 GHz). This is shown in Figure 3.2. According to this theory, radar measurements at P- and L-band may be affected by changes in the concentrations of solutes.

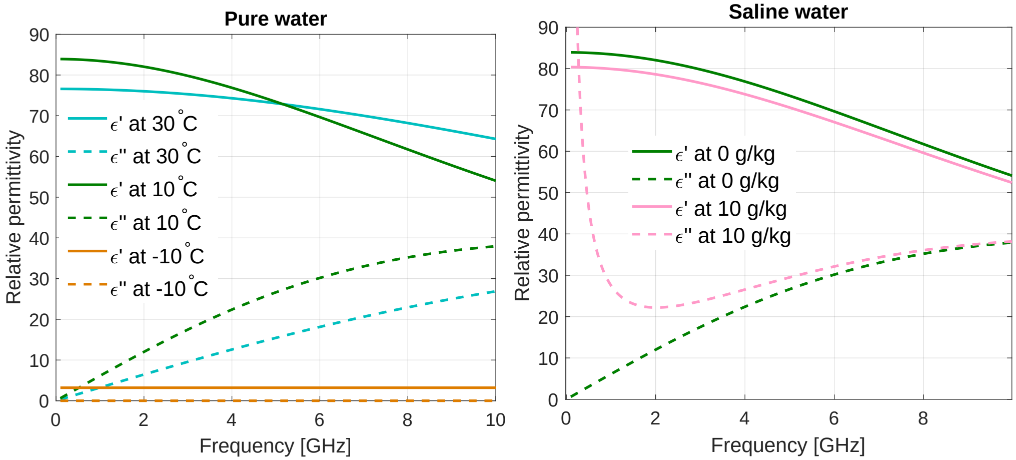

Figure 3.2. *Relative permittivity of pure water for different temperatures (left) and for pure and saline water at 10°C (right). Values for liquid water are based on the double-Debye dielectric model for saline water (Mätzler, 2006) and values for ice are based on the model reported in Hufford (1991).*

Permittivity of soil

Soil can be considered to be a mixture of soil particles, organic matter, water and air (Hallikainen et al., 1985). Soil particles are surrounded by a thin film of water which is tightly held by the surface of soil particles. These strong forces limit the rotation of water molecules, making this *bound water* behave similarly to ice in the presence of oscillating electromagnetic fields. Further away from the soil particles, *free water* is able to move through the soil medium with ease. The fraction of bound water making up the water content of a soil sample depends on the soil particle size distribution and mineralogy (e.g. sand, silt or clay). Smaller particle sizes, such as that of clay, have a larger effective surface area per unit volume, resulting in a larger fraction of bound water. Temporal variations in the permittivity of soil are mostly associated with variations in the temperature and volume fraction of free water in the soil.

The volumetric water content of forest soils may change with time due to precipitation, evaporation, transpiration, runoff and drainage (Parkin, 2008). Figure 3.3 shows that an increasing soil moisture content results in a significant increase in ϵ'. This is the basic principle behind soil moisture estimation using radar and passive microwave radiometers (Moghaddam, Saatchi, and Cuenca, 2000; Entekhabi et al., 2014). A higher soil moisture content results in stronger reflections of electromagnetic waves off ground surfaces. Backscatter at L-band and lower frequencies is also strongly correlated with soil salinity due to its sensitivity to ϵ'' (Yun Shao et al., 2003). Temperature has an equally significant effect on the relative permittivity of soil. Figure 3.3 shows that ϵ' drops rapidly as the temperature of the soil drops below 0°C, resulting in a large drop in ground backscatter (Pulliainen, Kurvonen, and Hallikainen, 1999). This drop is due to free water turning into ice (Hallikainen et al., 1985). Below 0°C, the relative permittivity is strongly dependent on temperature. Unlike pure water, not all water in soil freezes below 0°C. Instead, the fraction of frozen water increases as the temperature becomes more negative

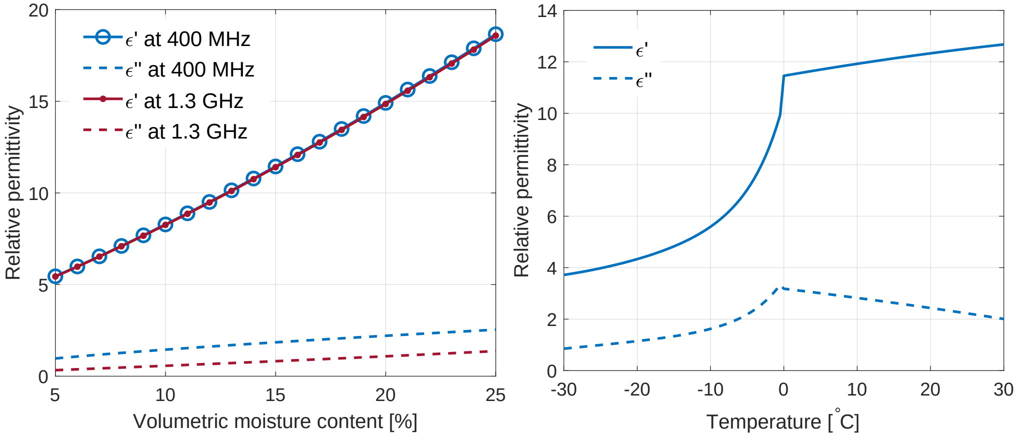

Figure 3.3. *Relative permittivity of mineral soil as a function of volumetric water content (left). These curves were computed using the model in Peplinski, Ulaby, and Dobson (1995) assuming sand, clay and silt mass fractions of 0.5, 0.15 and 0.35, respectively, at 20°C. The figure on the right shows the relative permittivity of organic soil at 1.4 GHz as a function of temperature. These curves were computed using the model and parameters in Mironov et al. (2019) assuming a volumetric water content of 34% and an organic matter content of 80%.*

(Tice, Black, and Berg, 1989). Air temperature variations for temperatures below 0°C will, therefore, cause variations in the ground backscatter. The effects of soil freezing and thawing on backscatter are different. Freezing of soil moisture occurs gradually, resulting in a gradual decline in surface backscatter (Wegmüller, 1990). Since the soil surface is exposed to air, an increase in air temperature to positive degrees will create a thawed soil layer at the top, causing backscatter to rapidly increase. Above 0°C, the relative permittivity of soil is weakly dependent on temperature. Temporal variations in the permittivity of soil above 0°C are, therefore, expected to occur due to changes in the moisture content instead.

Permittivity of wood

Living wood consists of cell walls (cellulose, hemicellulose and lignin), air, bound water and free water (Torgovnikov, 1993). As with soil, the dielectric properties of wood are mainly determined by the permittivity and volume fraction of free water. The properties of bound water, which resides in cell walls, are poorly understood. The dependencies of the relative permittivity of wood on frequency, temperature and moisture content share similarities with those of soil. At negative temperatures, a fraction of the water in wood turns into ice. The rest of the water remains unfrozen in a supercooled state. As with soil, freezing results in a large drop in permittivity (Mavrovic et al., 2018). An increase in water content results in an increase in ϵ' and ϵ'' (Salas et al., 1994). Within the range of values found in nature, an increase in ϵ' results in a stronger forest backscatter, whereas an increase in ϵ'' results in a slight drop in backscatter due to increased absorption (Moghaddam, Durden, and Zebker, 1994; Moghaddam and Saatchi, 1999). In general, wood is not an isotropic material, i.e. its permittivity is not the same in all directions and can be modelled as a tensor field. Water columns existing in elongated cells along the axial direction of the tree stem result in ϵ' being higher than that in the radial/tangential direction by a factor of 1.5 to 2 at P- to X-band (Torgovnikov, 1993). These phenomena are shown in Figure 3.4.

In situ measurements have shown that the permittivity of living wood varies with time. It has been observed that ϵ' of living wood is correlated with soil moisture, precipitation events and air temperature (Zimmermann et al., 1995; McDonald et al., 1999; McDonald, Zimmermann, and Kimball, 2002; Watanabe et al., 2015; Mavrovic et al., 2018). Perhaps the most interesting dynamics in tree permittivity that have been observed are diurnal cycles during warm periods. Diurnal cycles in ϵ' and ϵ'' are correlated with air temperature. Since there is no significant experimentally-observed relationship between wood permittivity and temperatures above 0°C (Zimmermann et al., 1995), the prevailing hypothesis is that the observed diurnal cycles in permittivity are due to diurnal cycles in tree water content. This establishes a link between radar measurements and biological mechanisms affecting tree water content. These mechanisms are explored in the following chapter.

The reported influence of solutes on the permittivity of wood, in particular ϵ'', is inconsistent in literature. In McDonald, Zimmermann, and Kimball (2002) it was postulated that temporal variations observed in the P-band permittivity of tree stems were partly due to variations in the concentrations of amino acids and potassium, resulting in ionic conduction and a change in the free-to-bound water ratio. Watanabe et al. (2015) state that zero salinity, and thus no ionic conduction, is expected in tree sap because salt prevents crops from growing. Moisture extracted from trees by Torgovnikov (1993) showed that the dielectric properties of free water does not practically differ from those of pure water. Moisture extracted from corn stalks in Ulaby and Jedlicka (1984) showed significant amounts of dissolved NaCl. However, the dielectric properties of intact corn stalks did not show the increase in ϵ'' at lower frequencies that is characteristic of saline water (see Figure 3.2). This discrepancy was believed to be due to the destructive nature of free water extraction, destroying the cell structure containing solid salts or salts dissolved in bound water. A comparison of the measured relative permittivity of living wood and that of the excised wood samples have also shown significant differences (Kalinkevich, 2013). It is, therefore, currently uncertain to what extent (if at all) concentrations of solutes in tree tissues affect the electric permittivity of wood.

The permittivity varies along the radius and height of tree trunks (Kalinkevich, 2013). This complicates electromagnetic modelling of forest scattering since point measurements provide limited information about the distribution of permittivity in trunks. Several studies show that ϵ' and ϵ'' are higher towards the outer edge of stems (Salas et al., 1994; McDonald, Zimmermann, and Kimball, 2002; Mavrovic et al., 2018), while in El-rayes and Ulaby (1987), the opposite was observed. The distribution of permittivity in branches is even less well understood.

The major limitation in our understanding of the dielectric properties of trees is the difficulty of measurements. Other than the issues already discussed, the measurements are highly sensitive to air gaps between the sensor and sample. *In situ* measurements are invasive, and trees respond to wounds over time, making time series measurements difficult. Calibration of the instruments is difficult and the instruments themselves are expensive, limiting the spatial diversity of simultaneous measurements. Cheaper, non-invasive methods for measuring the *in situ* permittivity of trees are needed.

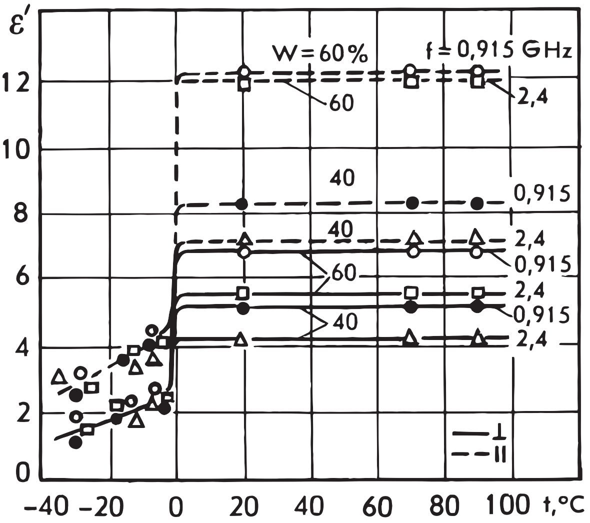

Figure 3.4. *Relative permittivity (real part) of spruce wood (species not specified) as a function of temperature for different moisture contents (*W*) and frequencies (*f*) of 0.915 GHz and 2.4 GHz. Curves are shown for field directions perpendicular to the stem axis ($\perp$) and along the stem axis ($\|$). Reproduced, with permission, from Torgovnikov (1993).*

3.3 Scattering mechanisms

A scattering mechanism is a description of how electromagnetic fields interact with scatterers during a radar measurement. In addition to the previously described dielectric properties, a scattering mechanism is affected by the frequency, polarisation and incidence angle of the incident electromagnetic wave. Different structures, such as tree trunks and canopies, have different scattering mechanisms, which are important to understand when designing forest parameter estimation algorithms. Scattering mechanisms are important in this thesis because of the following hypothesis: *temporal variations in radar observables at different frequencies, polarisations and heights within the forest canopy provide information about the scattering mechanisms taking place in the forest.*

Effects of polarisation on scattering

Polarisation differences in scattering mechanisms exist because the electric field radiated by an elemental current does not have the same magnitude in all directions relative to the direction of the current density. If the directions in which the electric field is strongly radiated by an elemental current coincide with directions in which the fields scattered from an object add constructively, the total scattered field has a large magnitude. When these directions are not aligned, the scattered field has a small magnitude. This causes differences in not only the polarisations, but also magnitudes of scattered fields for different polarisations of incident fields. A consequence of this phenomenon is the *Brewster effect*, in which specular reflections off smooth horizontal surfaces are stronger for H-polarised waves than for V-polarised waves. As a result, double-bounce scattering (ground-trunk and trunk-ground) at VV is less strong than at HH (Dobson et al., 1992; Moghaddam and Saatchi, 1995). Multiple scattering plays an important role in scattering differences at different polarisations. The strong double-bounce scattering mechanism dominates co-polarised (HH and VV) backscatter at P- and L-band in boreal forests (Richards, Sun, and Simonett, 1987; Moghaddam and Saatchi, 1995). Cross-polarised (HV and VH) observations mainly originate from multiple scattering between randomly oriented scatterers, such as branches in the forest canopy. A tilted tree trunk over a ground surface can also produce a strong cross-polarised scattering component (Chiu and Sarabandi, 1999; Smith-Jonforsen, Ulander, and Luo, 2005). Different polarisations, thus, provide different information about the forest structure, which is the basis of SAR polarimetry.

Effects of frequency on scattering

For objects that are small relative to the wavelength, such as small twigs and needles/leaves, the phases of currents induced in the scatterer ($\boldsymbol{J}(\boldsymbol{r}')$ in (3.1)) are approximately equal (Solimini, 2016). As a result, fields do not add constructively in any particular direction, resulting in *diffuse* scattering for a collection of small scatterers. The scattered power is proportional to f^4 (*Rayleigh scattering*), making it highly sensitive to the radar frequency (Bohren and Huffman, 1998). The electromagnetic energy scattered by the forest canopy also contributes to attenuation of the electromagnetic wave propagating into the canopy, reducing the scattering contributions of structures below the canopy. As a result, forest canopy constituents dominate C-band observations, but have little effect at P-band (Saatchi and Moghaddam, 2000).

Frequency also has an effect on the directivity[3] of the scattered field for objects that are large compared to the wavelength. For a dielectric cylinder, such as an idealised tree trunk, the smooth surface results in a strong specular component, resulting in the double-bounce scattering mechanism. Due to the finite length of a tree stem, power is also scattered in other directions, resulting in a direct (single bounce) scattering component off tree trunks (Sun, Simonett, and Strahler, 1991). While the double-bounce scattering component appears to originate from the ground level, the single-bounce scattering component will appear to originate from higher up in the canopy.

An opposite effect occurs for large rough surfaces, such as a forest floor. At low frequencies, a rough ground surface may appear smooth relative to the wavelength, resulting in strong specular reflections. A strong specular reflection from the ground will result in a strong double-bounce component, but little direct backscatter. At higher frequencies, a rough ground surface will scatter an incoming wave diffusely, resulting in a stronger direct backscattering component. However, the incoming wave undergoes greater attenuation by the canopy, making the direct ground scattering component small for all frequencies in forests (Moghaddam and Saatchi, 1995).

---

[3] Directivity is a measure of the concentration of a radiated field in a particular direction.

4

Tree water relations

The previous chapter has shown how water plays a significant role in electromagnetic scattering at microwave frequencies in forests. In this chapter, the biological processes affecting the water content in trees are introduced. These processes are species dependent. Focus is placed on Norway spruce (*Picea abies*), which together with Scots pine (*Pinus sylvestris*), are two species of evergreen conifers that dominate the boreal forests of Europe (Lindroth and Crill, 2011).

4.1 Tree anatomy

Water is taken up by the roots, travels through the trunk and is released into the atmosphere by needles. The trunk consists of several concentric layers (see Figure 4.1). Water is transported upwards within the *sapwood*, which forms the outermost layer of wood in the stem. The sapwood thickness relative to the heartwood radius depends on age and access to solar radiation (Sellin, 1994). Sapwood is formed on the perimeter of the stem by the *cambium*. The old, innermost sapwood loses its water carrying capability and becomes *heartwood*, which provides structural support. Heartwood and sapwood can often be distinguished by a change in colour (as in Figure 4.1), although they are visually indistinguishable in Norway spruce. The water-carrying tissue supporting water moving from roots to needles in the sapwood is called the *xylem*, which contains most of the water in a tree. In conifers, water passes through elongated cells in the xylem, called *tracheids*, that conduct water from roots to needles (Bowes, 2010). Tracheids are dead, rigid cells that are connected to neighbouring tracheids via holes, forming a hydraulic pathway from root to needle (Hölttä et al., 2013). Water exits the needles as water vapour through openings called *stomata*. The bark can be subdivided into the inner living layer, called the *phloem*, and the dead outer bark. The phloem transports sugars and other nutrients from needles to the rest of the tree. The flow rate in phloem is slower than that in the xylem. The phloem is elastic, allowing changes in volume. Water can flow between the xylem and phloem via radially arranged *ray cells* in the stem (Sevanto, Hölttä, and Holbrook, 2011; Pfautsch et al., 2015).

4.2 Transpiration

Sequestration of carbon by trees comes at the cost of losing large amounts of water to the atmosphere. Transpiration is the process in which water that has been taken up from the soil by the roots evaporates into the atmosphere through the stomata. The driving force of this water transport is the difference in water potential[1] between water vapour at the needle surface and water in the soil (Crang, Lyons-Sobaski, and Wise, 2018).

---

[1] Water potential is the potential energy of water per unit volume relative to pure, free water at ground level, at atmospheric pressure and at 298 K. More simply, water potential can be thought of as a pressure, in which water flows from higher to lower pressures (Hirons and Thomas, 2017).

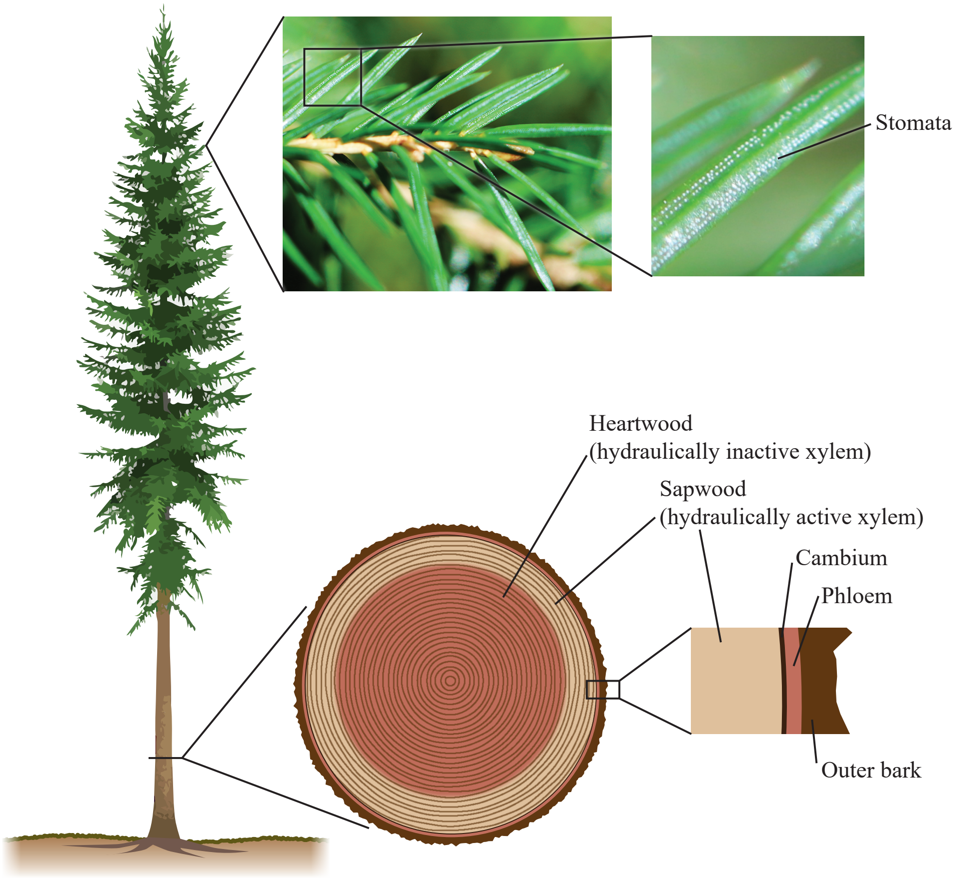

Figure 4.1. *Illustration of the Norway spruce anatomy. Photo of Norway spruce needles by Céline Heuzé.*

The cohesion-tension theory

The most widely-accepted description of how water moves through a tree is the *cohesion-tension theory* (Dixon and Joly, 1894; Tyree and Zimmermann, 2002; Brown, 2013). This theory states that water moves as continuous columns of water through interconnected tracheids in the xylem. This is possible because of the permanent dipoles of water molecules forming hydrogen bonds. Hydrogen bonds cause water molecules to hold on to each other (*cohesion*), as well as to polar materials such as the walls of tracheids (*adhesion*). During the day, the water column is pulled up by the atmosphere as water evaporates and leaves the stomata. Water lost to transpiration is replaced by water uptake by the roots. During the night, when evaporation stops, the column of water is held within the tree until evaporation resumes in the morning.

The most remarkable feature of tall trees must be their ability to support and transport water under immense tension, without any mechanical pumping action, which even a vacuum cannot create. However, if this tension becomes too high (due to rapid evaporation or too little soil moisture) a water column will break apart. Although such *cavitation* is partly reversible, conifers are adapted to minimise this damage. By regulating the size of stomatal openings, conifers can regulate the rate of evaporation. It has been observed that when the soil moisture content dropped to below approximately 20%, the rate of transpiration began to decrease due to stomatal regulation (Lagergren and Lindroth, 2002). By varying the diameter of tracheids throughout the growing season (forming tree rings), conifers can make water columns more robust to cavitation at the cost of reducing the rate of transpiration (Crang, Lyons-Sobaski, and Wise, 2018). However, it is in the tree's metabolic interest to have a rate of transpiration as high as possible. Trees have another adaptation which serves this purpose: water storage.

Water storage in trees

Water within tree tissues such as xylem and phloem can be used for transpiration during periods of high evaporative demand (Steppe, Sterck, and Deslauriers, 2015; Pfautsch, Hölttä, and Mencuccini, 2015; Landsberg, Waring, and Ryan, 2017). During the day, the rate of transpiration exceeds the rate of ground water uptake, decreasing the volume of water within tree tissues. Water reserves are replenished in the late afternoon to the early morning when the rate of ground water uptake exceeds the rate of transpiration. In Norway spruce, most of this depletable water is stored in the needles and phloem (Zweifel and Häsler, 2001; Zweifel, Item, and Häsler, 2001; Pfautsch, Hölttä, and Mencuccini, 2015). Diurnal changes in bark thickness due to changes in water content are measurable as a diurnal pulse in the stem radius. The process of diurnal variation in water content is illustrated in Figure 4.2. Water in the bark serves as a buffer to regulate the xylem water tension under varying soil moisture and atmospheric conditions (Landsberg, Waring, and Ryan, 2017). This mechanism is essential for efficient transpiration in tall trees while minimising cavitation. Stored water can be used to maintain transpiration for several days during dry conditions (Čermák et al., 2007). Water stored in the bark also plays a role in protecting the xylem from cavitation during freezing events (Zweifel and Häsler, 2000).

As discussed in the previous chapter, the electric permittivity of wood is dependent on the volumetric water content. Diurnal variations in stem water content, therefore, result in diurnal variations in permittivity as observed in McDonald, Zimmermann, and Kimball (2002), Watanabe et al. (2015) and Mavrovic et al. (2018). The lower stem supplies the largest volume of stored water, but the volumetric water content taken from storage during the day increases with height (Zweifel, Item, and Häsler, 2001; Sevanto et al., 2002; Čermák et al., 2007; McCulloh et al., 2014). Diurnal variations in satellite-based forest backcatter measurements have been observed as differences of 0.5 to 2 dB between morning and evening overpasses (Birrer et al., 1982; Satake and Hanado, 2004; Frolking et al., 2011; Friesen et al., 2007; van Emmerik et al., 2017). A simulation study by Steele-Dunne, Friesen, and van de Giesen (2012) showed that changes in vegetation water content are capable of causing the observed backscatter variations. A diurnally varying water tension may also affect the permittivity (Salas et al., 1994), although this hypothesis has not been further explored. The decrease in stem water content is primarily driven by the rate of transpiration in relation to soil water availability. The rate of transpiration is further determined by a complex interaction of several biotic and abiotic factors.

4.3 Factors affecting the rate of transpiration

Vapour pressure deficit

The vapour pressure deficit (VPD) is the difference between the vapour pressure within the stomata and the vapour pressure in the surrounding air. It is usually assumed that the air within the stomata is saturated (100% relative humidity). VPD is a measure of drying power, and a driver of transpiration (Monteith and Unsworth, 2013). VPD can be estimated from meteorological data as $\text{VPD} = e_{\text{sat}}(T)\,(1 - \text{RH}/100)$, where $e_{\text{sat}}(T)$ is the saturation vapour pressure, T is the air temperature and RH is the relative humidity in the air (Abtew and Melesse, 2013). The saturation vapour pressure is temperature dependent and can be estimated using several methods, e.g. using the Goff–Gratch equation (Goff, 1946). The VPD is high when the air temperature is high and relative humidity is low. These conditions typically occur during hot summer days, resulting in a high evaporative demand, high rate of transpiration and a significant drop in tree water content. Diurnal cycles in VPD were clearly correlated with diurnal cycles in permittivity in McDonald, Zimmermann, and Kimball (2002). During cold or wet conditions, the VPD is low, resulting in low rates of transpiration.

Stomatal conductance

Stomatal openings can be mechanically varied, limiting the loss of water through transpiration. *Stomatal conductance* describes how easily water vapour can exit a needle and enter the atmosphere. During hot days, when the evaporative demand is very high, the stomata may partially close, limiting the loss of water and avoiding cavitation (Zweifel, Böhm, and Häsler, 2002; Hirons and Thomas, 2017). This *mid-day stomatal closure* can be observed as a temporary drop in sap flow rate in the stem. Stomatal conductance is a function of solar irradiance, atmospheric CO_2 concentration, VPD, leaf temperature, and soil water potential (Jarvis, 1976; Landsberg, Waring, and Ryan, 2017). Feedback loops in the control of transpiration are introduced by variations in stomatal conductance. Several models have been developed with the aim of predicting stomatal conductance given measurable physical quantities (Damour et al., 2010).

Wind speed

Stronger winds result in higher rates of evaporation from an air-water interface. The *boundary layer conductance* of a conifer needle describes how easily water vapour can be transported from a stomatal opening to the atmosphere. The boundary layer conductance is proportional to the square root of the wind speed at the needle surface (Campbell and Norman, 1998). For a large stomatal conductance, an increase in wind speed results in an increase in transpiration rate. It can, thus, be expected that wind speed has a significant influence on the rate of transpiration during summer conditions. This has been observed in a controlled wind tunnel experiment (Chu et al., 2008). The presence of wind affects the needle temperature and VPD at the surface of the stomata, to which the stomata may respond by reducing the stomatal conductance (Jarvis and McNaughton, 1986). The effects of wind on transpiration are, therefore, only observed when the solar irradiance is sufficiently high and if there is sufficient water available to supply a high rate of transpiration (Daudet et al., 1999).

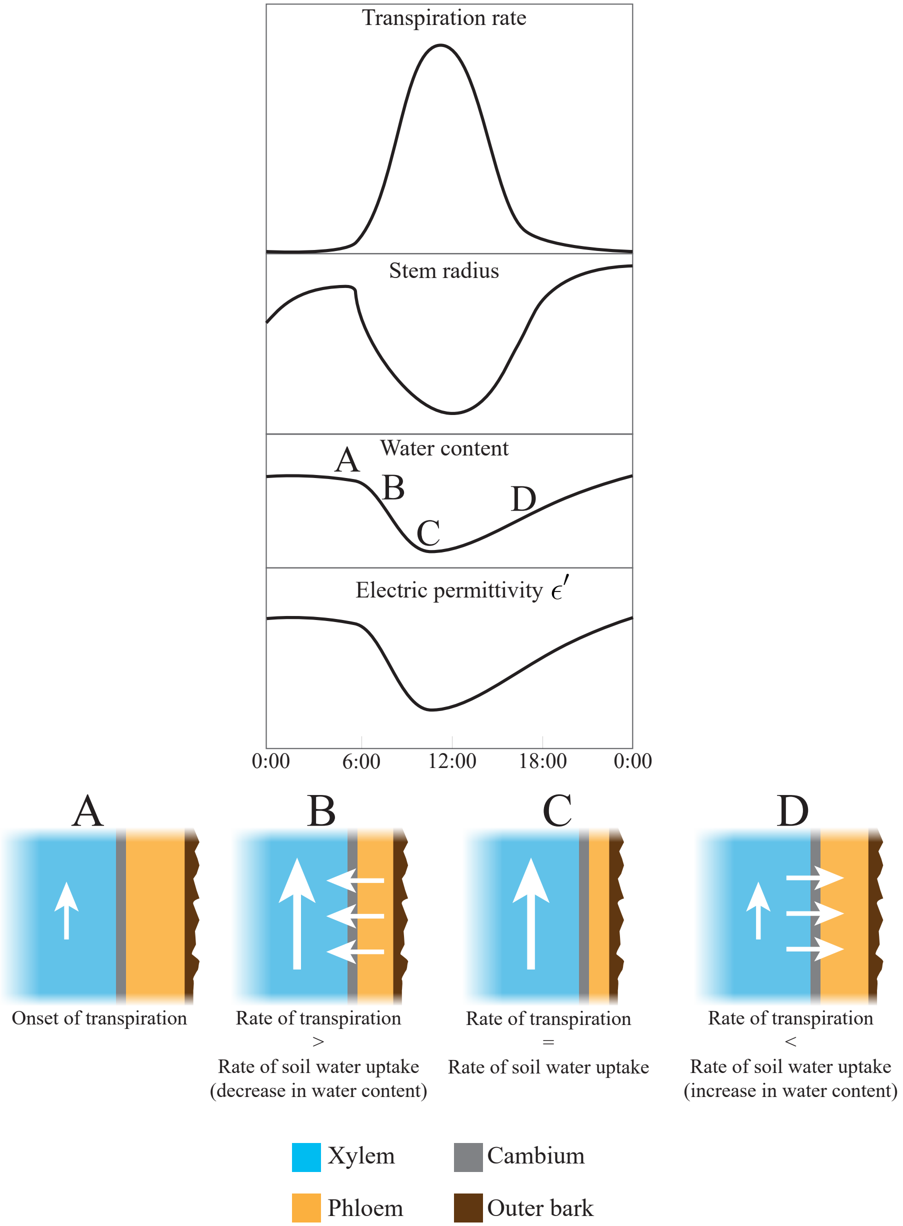

Figure 4.2. *Conceptual description of the diurnal cycle in transpiration rate, stem water content, stem radius and electric permittivity of the stem. White arrows indicate the magnitude and direction of water flow between tissues in the stem at different times of the day. The illustrations are based on similar illustrations in Herzog and Thum (1995), Pfautsch, Hölttä, and Mencuccini (2015) and Steppe, Sterck, and Deslauriers (2015). The permittivity curve is based on observations in McDonald, Zimmermann, and Kimball (2002).*

The BorealScat experiment

5

This chapter introduces the experiment carried out in this thesis. Some design challenges are detailed which are not treated in the appended publications, and an overview of the data analysis methods is given.

5.1 Experiment goals

The goal of the BorealScat experiment was to study temporal variations in radar backscatter and temporal coherence of a boreal forest at multiple frequencies, polarisations and heights within the forest. A better understanding of these temporal variations in radar observables is beneficial for the design of forest parameter estimation algorithms and the design of future spaceborne SAR missions. It was expected that the results would reveal new insights about the influence of seasons, weather variables, moisture variations and the electromagnetic scattering mechanisms taking place in boreal forests during SAR observations. Tomographic radar observations with a fine temporal resolution were carried out over several years to capture temporal changes in the radar observations over a wide range of timescales. This required a fully automated, fixed, tower-based radar observing a scene representative of boreal forests.

5.2 Forest site

The Remningstorp experimental forest in southern Sweden was chosen for the BorealScat experiment. Remningstorp consists of many forest stands of varying tree density, biomass and species. The forest is regularly inventoried, and it was the subject of several previous radar remote sensing studies, including the BIOSAR airborne campaigns in 2007 and 2010 (Hajnsek et al., 2008; Ulander et al., 2011). A forest stand was chosen based on accessibility by road, access to electricity, representativeness of boreal forests and type of terrain. Space for an unobstructed trihedral corner reflector, at a suitable distance from the radar, was also a requirement. The chosen stand is a dense forest of mature Norway spruce, which is a well-studied species in terms of physiology and a common boreal species. Tree heights in the stand vary from approximately 25 m to 27 m with an above-ground biomass of 250 tons/ha as estimated in the fall of 2014 from ground inventory measurements. The ground is covered in moss, has little understory, and is mostly flat. The flat terrain was chosen such that double-bounce scattering, which dominates most boreal forest radar observations, could be observed. Figure 5.1 shows an illustration of the experiment site.

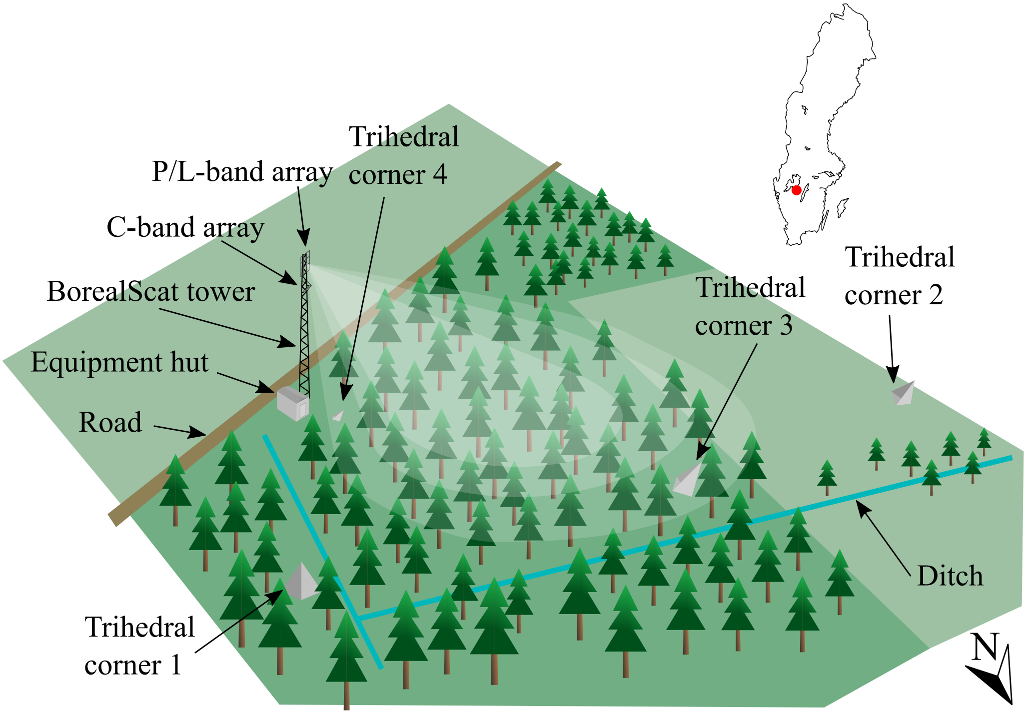

Figure 5.1. *Illustration of the BorealScat experiment site located in Remningstorp, Sweden. The illuminated region corresponds to the P/L-band region of illumination. The C-band region of illumination is not shown. Trihedral corner reflectors 1 to 3 have short sides of 5.1 m, whereas trihedral corner reflector 4 has a short side of 70 cm. Reflector 3 is concealed in the forest, whereas the others are in direct line of sight of the antennas.*

5.3 Experiment design

The tower

The purpose of the 50 m high tower (Figure 5.2) was to mount the antennas at a height that is several wavelengths from the nearest forest scatterers, to allow observation of the forest at similar incidence angles as in spaceborne SARs (20° to 55°), and to offer a large field of view for several years. A requirement of the tower was that the antennas should not move by more than ±3 cm up to wind speeds of 17 m/s to minimize system decorrelation. Another requirement was that the tower should be free standing to avoid reflections from guy wires supporting the tower. This required a tower with a sturdier metal frame and larger concrete foundation than what is normally necessary for a tower of this height. Structural simulations of the tower, accounting for the estimated weight, wind loading and ice cover of all tower elements, were run by the tower manufacturer to ensure that the tower displacement due to wind was within the required range.

Figure 5.2. *Photo of the radar tower soon after construction. The equipment hut can be seen at the base of the tower. Only the P/L-band system was installed at the time.*

Antenna arrays

To acquire tomographic images of the forest, measurements from multiple incidence angles were necessary. Some ground-based systems implement this by mechanically moving an antenna over a synthetic aperture (Morrison and Bennett, 2014; Frey, Werner, and Wiesmann, 2015). This approach has the advantage that the incidence angle can be constant across the image. This solution was not feasible due to maintenance requirements[1] and the fact that the trees would move during this mechanical movement of the antenna, resulting in blurred tomographic images. A fixed antenna array design was chosen to avoid temporal decorrelation during the tomographic measurement sequence. The geometric configuration of antennas in the array needed to satisfy several requirements:

---

[1] Regulations against tower climbing in Sweden required that anything mounted on the tower had to be designed for minimal maintenance.

1. Provide sufficient vertical resolution to distinguish between scattering in the upper canopy and ground layers.
2. Provide unambiguous imaging over the full height of the forest.
3. Measure at all four linear polarisation combinations.
4. Measure at P-, L- and C-band.

As described in Paper I, the virtual array principle was used with suitable antennas to cover the required polarisations and frequencies. The virtual array principle allows virtual array elements to be sufficiently closely spaced when the physical dimensions of the antennas are too large for the spacing requirement. Vertical columns of 5 transmitting antennas and 5 receiving antennas yield 25 closely spaced virtual elements. Some virtual elements may overlap, and only part of the virtual array is regularly spaced. Figure 5.3 shows the positions of virtual array elements relative to the physical antennas. Close spacing of array elements is necessary for a sufficiently large height of ambiguity. The total vertical extent of the array determines the resolution in elevation. The resolution in elevation is also dependent on the angle off boresight of the array, being finest at boresight. A tilted array, placing the forest at the array boresight, would provide the finest spatial resolution over the forest. However, the antennas chosen for P- to L-band measurements had a wide lobe in azimuth (60° to 100°). This defines the spatial extent of the resolution cell in azimuth, since the virtual antenna array does not have multiple elements in the horizontal direction to provide a fine resolution in azimuth. The P/L-band array was designed such that it can be tilted at different angles relative to the tower by adjusting the long screws extending behind the array as can be seen in Figure 5.3. However, the resolution cell of a tilted array would be a tube curved over several heights, mixing the scattering contribution from different heights and worsening the vertical resolution (Morrison, Bennett, and Solberg, 2013). At installation, the array was mounted vertically, and was never tilted in order to avoid mixing reflections from different heights.

The choice of vertical spacing between antennas is a trade-off between vertical resolution and height of ambiguity. Closer vertical spacing of the antennas results in better vertical resolution, but decreases the height of ambiguity. For a fixed antenna array geometry, an increase in radar frequency results in better vertical resolution, but a lower height of ambiguity. The array requirements become more difficult to satisfy for wider frequency ranges. For columns of 5 antennas, the vertical resolution and ambiguity requirements could not be met from P- to C-band. A separate antenna array was necessary for C-band measurements to meet the requirements. This presented an opportunity for compensating for the high cable losses at C-band (13 dB one-way loss compared to 5 dB at L-band). The antenna gain was increased by choosing an antenna with a small beamwidth in azimuth (10°). A small azimuth beamwidth also meant that a tilted array would not mix reflections from different heights. This allowed the array to be tilted, providing the maximum resolution in elevation over the forest. Unlike the P/L-band antennas that were pointed horizontally from the tower, the C-band antennas were pointed towards the forest, placing the forest in the region of highest antenna gain.

The spatial extent of the forest scene is on the order of the distance between the radar and the scene. As a result, the relationships between the antenna array geometry and measures such as vertical resolution and height of ambiguity are not as simple as in spaceborne SAR tomography. The vertical resolution and height of ambiguity vary across the imaging plane. Different antenna array geometry designs were evaluated by simulating a scene of point scatterers. The simulation

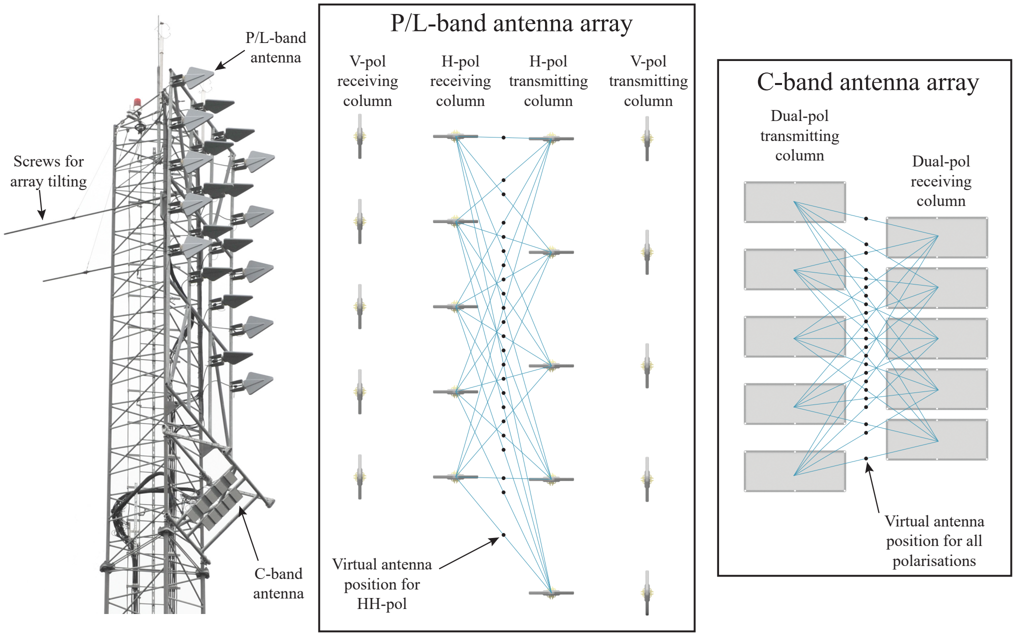

Figure 5.3. *Illustration of the virtual antenna array concept for the P- and L-band antenna array (middle) and the C-band antenna array (right). Both arrays are viewed from the front. Blue lines connect transmitting and receiving antenna pairs. Virtual antenna positions lie halfway between the transmitting and receiving antennas.*

accounted for the antenna array geometry and 3D antenna gain patterns, which were provided by the manufacturers. Figure 5.4 shows examples of simulated tomograms for the final array designs using 4000 point scatterers with a maximum height of 30 m. Ambiguous responses are seen in both L- and C-band tomograms, but appear above the forest height and are, thus, not a problem. Due to the wider bandwidths and larger antenna array apertures relative to the wavelength, the spatial resolutions for L- and C-band are significantly better compared to that of P-band.

The antennas were chosen to be resistant to moisture intrusion. The antennas had bulkhead connectors and radomes. All connections on the tower were further sealed using vulcanising tape. Nevertheless, moisture intrusion was observed in some of the C-band antennas. In mid-2019, all C-band antennas were replaced with a more weather-resistant model with the same electrical specifications. Connections were sealed using silicone and the array frame was modified to avoid the collection of water near the antenna connectors. Evidence of moisture intrusion was still seen in some of the C-band antennas. Moisture intrusion had the effect of varying the antenna gain and antenna pattern, and thus great care must be taken when interpreting the data. The C-band results presented in this thesis were taken from periods when moisture intrusion effects were negligible. This could be seen in the direct coupling response between antennas and the trihedral corner reflector response.

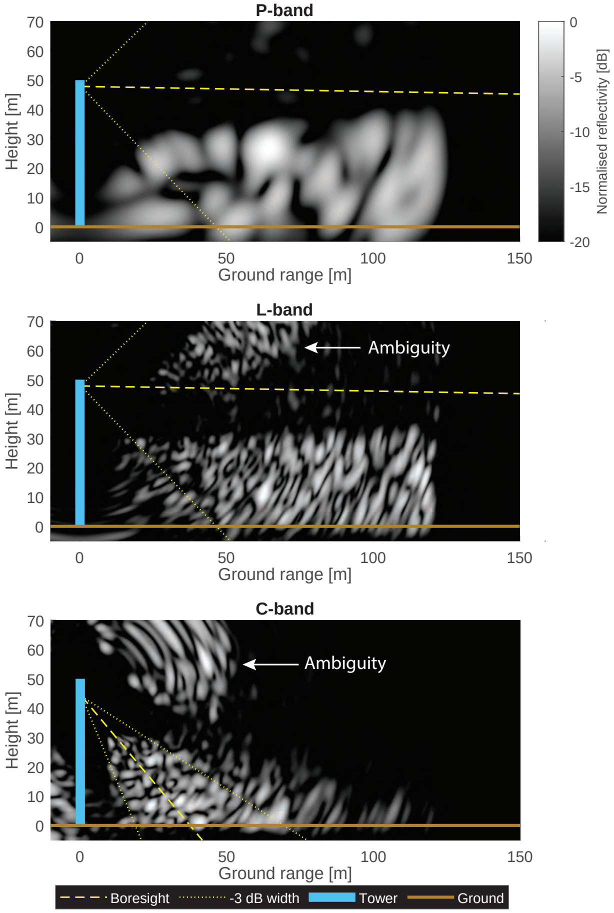

Figure 5.4. *Examples of simulated tomograms for the final antenna array designs. Ambiguous forest responses are seen above the 'forest' for L- and C-band. The effects of canopy attenuation and multiple scattering were not included in the simulation.*

Vector network analyser

A vector network analyser (VNA) was selected to serve as a transmitter and receiver. A VNA measures the amplitude ratio and phase shift between the transmitted and received unmodulated continuous-wave pulses. By stepping over a range of frequencies, called a *frequency sweep*, a finite bandwidth B can be covered (see Figure 5.5). The frequency step size Δf determines the unambiguous range

$$R_u = \frac{c_0}{2\Delta f}, \tag{5.1}$$

and B determines the range resolution

$$\delta_r = \frac{c_0}{2B}, \tag{5.2}$$

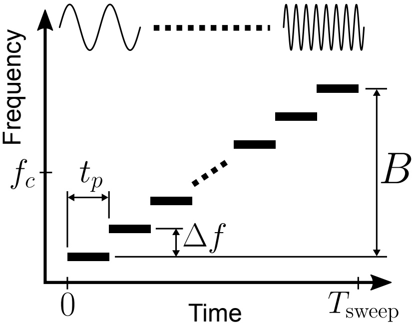

Figure 5.5. *Instantaneous frequencies of the waveform that is emitted by a VNA. Several monochromatic pulses with duration* t_p *are emitted in sequence with increasing frequencies (steps of* Δf*) to cover a bandwidth* B*. The duration of the frequency sweep is* T_{sweep}*. The centre frequency of the sweep is* f_c*.*

if the effects of tapering windows are ignored. VNAs are typically capable of measuring over several gigahertz, making them ideal for performing finite-bandwidth measurements at different centre frequencies, namely P-, L- and C-band. Commonly used in laboratory environments for testing a variety of electronic components, VNAs allow easy reconfiguration of their sweep parameters. Due to their narrow instantaneous bandwidth (10 kHz for BorealScat), VNAs have a high dynamic range. This results in a high SNR even for a low output power, which may be necessary for obtaining a permit to transmit within the desired frequency bands. A VNA-based radar is a more cost-effective solution for wideband measurements than a pulsed radar, but the narrow instantaneous input bandwidth makes measurements much slower. This poses a problem for tomographic measurements, where several frequency sweeps are necessary (one sweep per transmit-receive antenna pair) for a single tomographic image. The combined measurement time of all the sweeps is long enough for the forest to sway in the wind during measurements, resulting in blurred tomograms. To reduce the measurement time, sweeps were parallelised using a multiport VNA. A multiport VNA is capable of transmitting from a single antenna while receiving from all ports simultaneously. Paper I details the advantages of a multiport VNA over a conventional 2-port VNA for tomographic measurements.

Measurement sequence

Transmit-receive measurements were acquired along the vertical aperture created by the antenna array for reconstructing tomographic images. Such measurements were repeated for different transmit and receive polarisations and frequency bands to obtain a tomographic image for each polarisation and frequency band. This entire process was consecutively repeated in a burst of four measurements to increase the number of looks. Bursts were separated by 5 minutes. The order of events in a measurement sequence is illustrated in Figure 5.6. The time taken for a frequency sweep, T_{sweep}, depends on the signal bandwidth, which was different for each frequency band. The time taken for acquiring the data for a tomographic image, T_{tomog}, was therefore different for each band. Table 5.1 defines the frequency bands covered in a measurement sequence and gives their measurement times T_{sweep} and T_{tomog}.

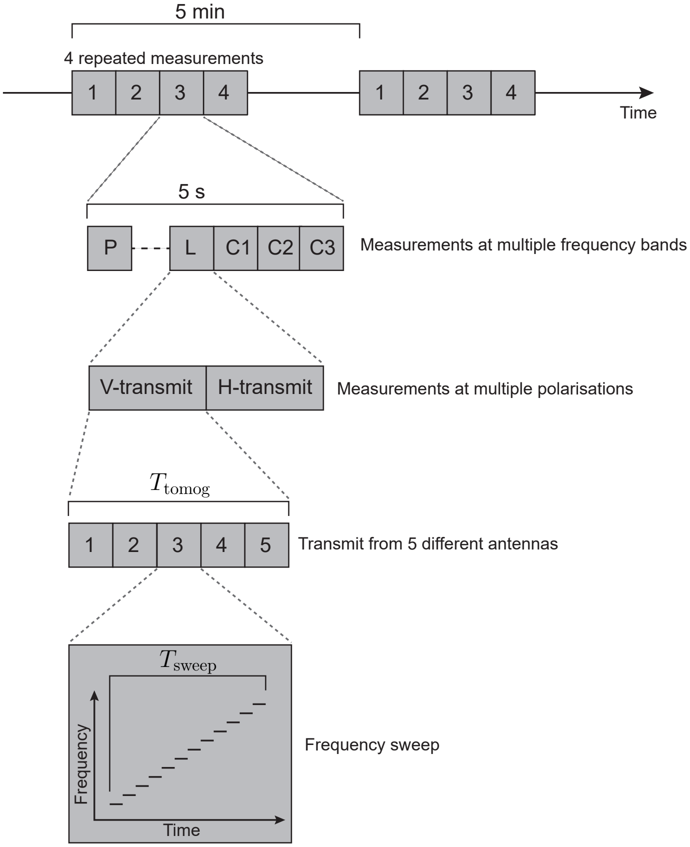

Figure 5.6. *Timing diagram of the measurement sequence. Delays due to data transfer and changes in the VNA configuration during the measurement sequence are not shown explicitly.*

As shown in Figure 5.6 and Table 5.1, the full bandwidth allocated for C-band measurements (320 MHz) was divided into three separate frequency bands. This was done to reduce temporal decorrelation during the tomographic measurement sequence. Temporal decorrelation during the measurement sequence is caused by trees swaying in the wind. The narrower bandwidth results in a shorter measurement time at the cost of a coarser range resolution. Another VNA configuration that was experimented with for reducing the measurement time was the instantaneous input bandwidth, commonly called the *intermediate frequency bandwidth* (IFBW). The amount of decorrelation decreases for a larger IFBW at the cost of a lower clutter-to-noise ratio (CNR). Figure 5.7 shows the results of an experiment with the goal of finding the VNA setting resulting in the least amount of decorrelation while maintaining a high CNR. The configuration with an IFBW of 10 kHz and a bandwidth of 106.5 MHz was chosen since temporal decorrelation was only seen at high instantaneous wind speeds (>8 m/s), while keeping the CNR at 16 dB.

After every burst of 4 tomographic measurements, continuous-wave Doppler measurements were carried out at P-band (435 MHz), L-band (1285 MHz) and C-band (5350 MHz). For each

Table 5.1. *Definitions of frequency bands covered in a measurement sequence, their sweep times* T_{sweep} *and tomogram measurement times* T_{tomog}.

Band	**Centre frequency [MHz]**	**Bandwidth [MHz]**	T_{sweep} **[ms]**	T_{tomog} **[ms]**
1 (P)	435	30	8	40
2	514	8	2	10
3	546	8	2	10
4	640	56	15	75
5 (L)	1307.5	135	36	180
6 (C1)	5303	106.5	28	140
7 (C2)	5410	106.5	28	140
8 (C3)	5516	106.5	28	140

frequency a continuous wave was transmitted for 10 s and sampled in time to resolve Doppler shifts due to radial velocities up to 15 m/s. The purpose of these measurements was to investigate sub-second decorrelation and Doppler spectra of the forest due to wind. Measurement results and clutter spectra models derived from the acquired data are published in Report D6 and are not within the scope of this thesis.

5.4 Analysis methods

Range profiles

The raw data measured by the VNA are complex-valued vectors specifying the magnitude ratios and phase shifts between transmit-receive ports of the VNA for different frequencies. The magnitudes are a function of losses in cables, the antenna gain patterns, free-space path loss, and backscatter from the forest scene. The phase shift between the transmitted and received continuous waves is a function of propagation delays in cables, propagation time in air and phase shifts caused by scatterers in the forest scene. These signals measured by the VNA radar are similar to the frequency-domain representation of a repetitive chirp signal, swept across the bandwidth B, after matched filtering, assuming a perfectly stable scene.

Reflections close to the antennas appear as low frequency complex sinusoids in the signal measured by the VNA. Reflections from objects far away from the antennas appear as high frequency complex sinusoids. Therefore, the inverse Fourier transform of the measured frequency-domain signal is a signal representing the complex reflectivity as a function of range. The frequencies in the VNA signal were regularly spaced, allowing the use of a fast Fourier transform algorithm to compute range profiles. The absolute square of this signal results in a measure of scattered power density as a function of range. An example of such a range profile is shown in Figure 5.8 for L-band, HH-polarisation. In Paper II, the forest region from range profiles were extracted to analyse the temporal evolution of forest backscatter and temporal coherence. However, scattering contributions from the upper canopy and ground regions cannot be separated from a single range profile.

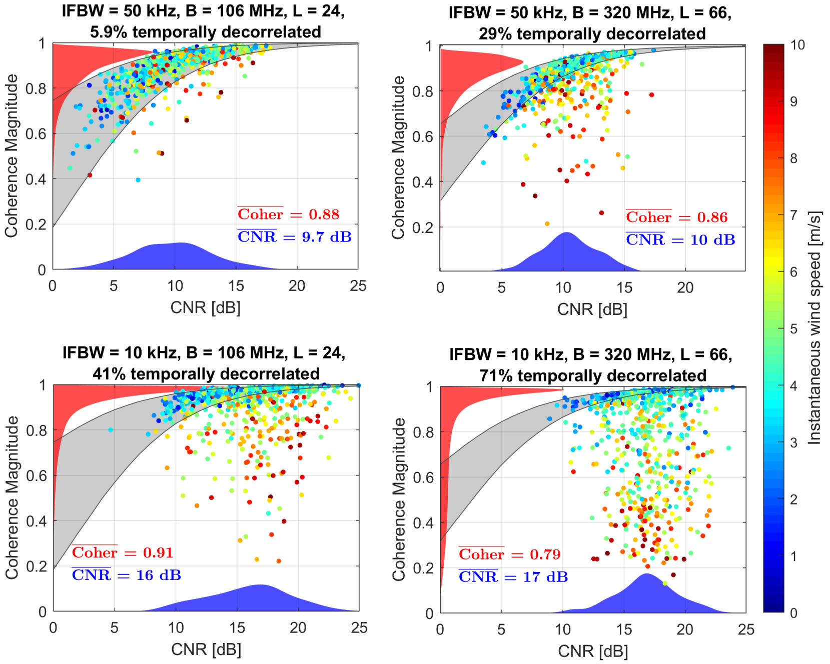

Figure 5.7. *Scatterplots showing the relationship between the coherence magnitude and CNR for C-band measurements over the timescale of the tomographic image measurement time for different VNA configurations. The different configurations are the instantaneous input bandwidth (IFBW) and the signal bandwidth (B). The grey region shows the 99% confidence interval of thermal coherence for the given number of looks (L). Any points below this region represents a measurement likely affected by temporal decorrelation. The blue region shows the CNR distribution and the red region shows the coherence distribution. The averages of these distributions,* $\overline{\text{Coher}}$ *and* $\overline{\text{CNR}}$*, respectively, are also given for each VNA configuration.*

Tomographic images

Tomographic images provide the complex reflectivity of the forest in the vertical plane. These images allow the analysis of the temporal evolution of backscatter and temporal coherence for different regions of the forest, e.g. the upper canopy, ground or the full forest (both canopy and ground). Constructing a tomographic image requires the coherent integration of complex-valued range profiles acquired from all combinations of 5 transmitting and 5 receiving antennas for a given polarisation combination. A complex-valued tomographic image $I(\mathbf{p})$ with pixels at positions in a 2D vertical plane denoted by $\mathbf{p}$ can be reconstructed through back-projection as

$$I(\mathbf{p}) = \sum_{m}\sum_{n} W_{El}(m,n) s_{mn}\left(\frac{R_m(\mathbf{p}) + R_n(\mathbf{p})}{2}\right) \exp\left(-j2\pi f_c \frac{R_m(\mathbf{p}) + R_n(\mathbf{p})}{c_0}\right), \tag{5.3}$$

where $R_m(\mathbf{p})$ and $R_n(\mathbf{p})$ are the distances between the point $\mathbf{p}$ on the 2D vertical image plane and the receiving antenna m and transmitting antenna n, respectively. $W_{El}(m,n)$ is a window

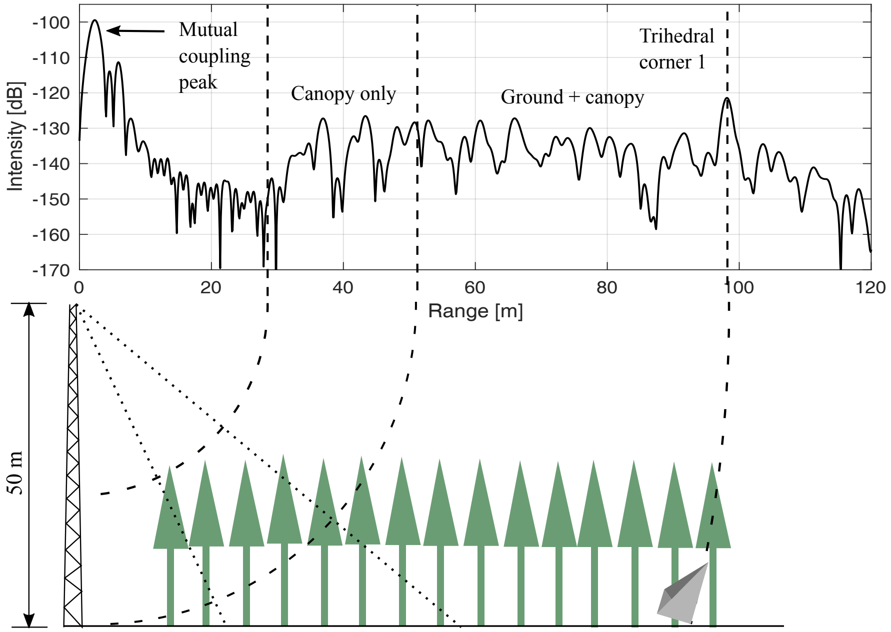

Figure 5.8. *Magnitude squared of a measured HH, L-band range profile with an illustration of how the range profile relates to a two-dimensional slice in the acquisition geometry. The dotted lines indicate the interval of incidence angles at ground level relevant to spaceborne SAR missions.*

function for suppressing sidelobes in elevation, which was chosen to be the Taylor window. The range profile s_{mn} is interpolated to the one-way range in its argument. The exponential term at the end is a phase correction which is necessary because image reconstruction is done at baseband, easing the requirements on spatial sampling and reducing the image reconstruction time. The magnitude-squared values of the pixels, i.e. $|I(\mathbf{p})|^2$, form an intensity image proportional to the forest backscatter.

As with SAR images, the tomographic images show a speckle pattern due to constructive and destructive interference between scattering elements in each resolution cell. This phenomenon makes it difficult to study temporal variations in the forest reflectivity. To obtain a reproducible estimate of backscatter or coherence, pixels in the tomographic image must be incoherently averaged or integrated to produce time series. The magnitude of speckle variations depends on the image resolution and size of the observed region. These variations can be significantly larger than some temporal variations in the forest backscatter. The effects of speckle variations are discussed in Paper IV.

5.5 Calibration

The limited field of view, near range observation geometry, close spacing of antennas, and limited bandwidth introduced new calibration challenges in the BorealScat experiment. The main goal of instrument calibration was to turn measured values into measures proportional to the true backscatter and phase. Since mainly temporal variations were of interest, calibrating the instrument in an absolute manner was not a priority.

It was important that significant temporal variations in the system's signal chain were compensated for. This ensures that the observed temporal variations in radar observables were due to changes in the observed scene. To assess the temporal stability of the radar instrument, two methods were used. First, a mechanical microwave switch was used to route each transmit port to each receive port via a reference cable. The VNA, switch and reference cable were all housed within a temperature-controlled instrument hut. These measurements would show any changes in VNA measurement characteristics over time. This internal calibration was done at least once every hour. No significant variations over the observation period were observed. Secondly, temporal changes in the response of the low-loss cables and antennas were assessed by observing changes in the direct coupling component between antennas (mutual coupling peak in Figure 5.8). Temporal variations in the direct coupling component were insignificant compared to the forest response, except during rain. As shown in Paper II, sharp peaks in the direct coupling component were seen during rain. When comparing these fluctuations with the signal from a corner reflector (shown in Figure 5.9), the fluctuations were only present in the direct coupling component. It was concluded that the fluctuation in the direct coupling component arise because they originate from sidelobes, which are more sensitive to moisture on the radomes than the mainlobe. Examples of these measures of temporal stability of the system are shown and discussed in Paper IV. It could, thus, be concluded that systematic variations were insignificant compared to variations in the forest reflection, and that a temporal calibration was not necessary.

With the knowledge that the system response was temporally stable, the remaining calibration steps were to

1. Suppress the mutual coupling component in P- and L-band measurements. This avoided tomographic image artefacts and allowed the use of a corner reflector for the following calibration step.

2. Compensate for magnitude and phase imbalances between antenna pairs contributing to a tomographic measurement. This produced focused tomographic images.

3. Compensate for the magnitude bias caused by a spatially variant impulse response. This prevented a weighting bias when extracting backscatter and coherence values over regions of interest in tomographic images.

New procedures developed for these three calibration tasks are detailed in Paper III.

Calibration step 2 was initially done using a contrast-based autofocus algorithm, whereby phase errors are estimated by maximising a particular image sharpness metric evaluated on the image intensity (Morrison, Do, and Munson, 2007). In Paper I, this was done by optimising a vector of phase corrections $\boldsymbol{\Phi}$ for maximum tomographic image contrast, which is a popular approach for SAR autofocus (Schulz, 2007). A single image involves contributions from 5 transmitting and 5 receiving antennas, giving 10 phase shift corrections to estimate. Only the

Figure 5.9. *Photo of the trihedral corner reflector used for calibration (Trihedral corner 2 in Figure 5.1).*

relative phases affect the image sharpness, therefore, one of the phase errors was set to 0 to serve as a reference phase. The phase correction vector $\mathbf{\Phi}$ consists of nine variable phase correction elements, requiring an optimisation over a nine-dimensional parameter space. Image contrast can be maximised by minimising the image entropy $H(\mathbf{\Phi})$. The optimisation problem for finding the optimal phase correction estimates $\hat{\mathbf{\Phi}}$ can be expressed as

$$\hat{\mathbf{\Phi}} = \arg\min_{\mathbf{\Phi}} H(\mathbf{\Phi}), \tag{5.4}$$

where the entropy is defined as

$$H\left(\mathbf{\Phi}\right) = -\sum_{\mathbf{p}} \mathrm{P}\left(\mathbf{p}, \mathbf{\Phi}\right) \ln \mathrm{P}\left(\mathbf{p}, \mathbf{\Phi}\right), \tag{5.5}$$

with normalised pixel intensity $\mathrm{P}\left(\mathbf{p}, \mathbf{\Phi}\right) = \left|I(\mathbf{p}, \mathbf{\Phi})\right|^2 / \sum_{\mathbf{p}} \left|I(\mathbf{p}, \mathbf{\Phi})\right|^2$. $I(\mathbf{p}, \mathbf{\Phi})$ is the complex tomogram reconstructed through back-projection after applying the phase shifts $\mathbf{\Phi}$ to the range profiles. The cost function $H\left(\mathbf{\Phi}\right)$ contains many local minima due to interference patterns arising from constructive and destructive interference, making it sensitive to environmental conditions. The algorithm also required hundreds of iterations, each of which required the construction of a tomographic image in order to derive a measure of the image contrast. The resulting tomograms would also have a random rotation, which needed to be manually corrected. Coherence-based tomographic calibration methods were investigated (Tebaldini et al., 2015), but the limited number of available looks resulted in poorly focused tomograms. The algorithm detailed in Paper III instead uses the reflection from a trihedral corner reflector that was installed in November 2017

(Figure 5.9). Relationships between transmit-receive antenna pairs were exploited to also calibrate cross-polarised channels using the same reflector. This calibration method was significantly faster than the autofocus method. It resulted in tomograms with no rotation and tomograms were consistently well focused regardless of environmental conditions.

5.6 Meteorological, moisture and biophysical data

A variety of sensors provided *in situ* data about the meteorological and moisture conditions. The location of these sensors in the experiment site are shown in Figure 5.10. Air temperature, relative humidity and pressure were measured at 2 m and 30 m above the ground. Precipitation was measured using a heated rain gauge, which cannot distinguish between rain and snow. Snow depth was not measured on site, but snow depth measurements were available from the nearby Remningstorp weather station. Two surveillance cameras provided qualitative snow cover observations of the canopy and ground. The 3D wind vector was measured using two ultrasonic anemometers at the top of the tower. These two ultrasonic anemometers were chosen for redundancy and minimal maintenance. Four soil moisture sensors were installed in the forest at the beginning of the experiment, of which three were destroyed by wildlife.

In mid-2019, two soil moisture pits were installed where soil moisture and temperature were measured at 5 cm depth intervals. A pyranometer, measuring the incoming solar radiation, was installed at the top of the tower. Three point dendrometers were installed on three separate trees. These dendrometers measure sub-micrometre variations in stem radius, showing not only tree growth but also diurnal water content variations (Zweifel, Item, and Häsler, 2001; Pfautsch, Hölttä, and Mencuccini, 2015). Two sap flow sensors were installed on each of these three trees. Sap flow sensors measure the vertical flow rate of xylem sap, which is closely related to the rate of transpiration (Čermák et al., 2007). Results from these sensors are shown in Paper V.

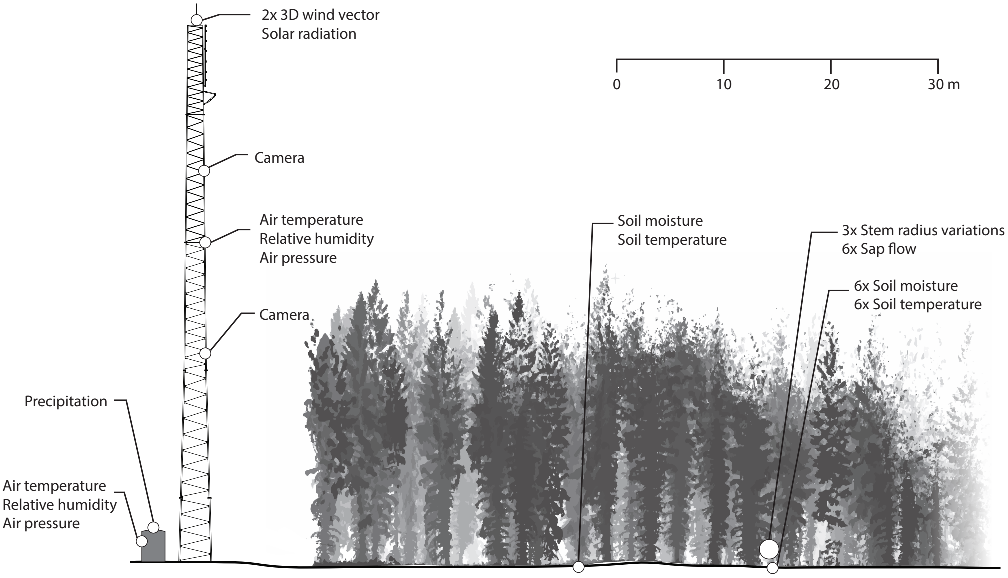

Figure 5.10. *Illustration (to scale) showing where meteorological, moisture and biophysical data were collected by sensors installed on site. The locations of two surveillance cameras are also shown.*

6 Summaries of appended papers

6.1 Paper I

Multiport Vector Network Analyzer Radar for Tomographic Forest Scattering Measurements

After the addition of C-band antennas on the tower in August 2017, the radar instrument installation was complete. This paper provides a first complete overview of the experiment setup, some design issues involved and the signal processing steps necessary for producing tomographic images. The first tomographic reconstructions from BorealScat data are demonstrated at P-, L- and C-band for the HH, HV and VV polarisations. Apart from C-band tomographic capabilities using an array radar, the system was novel in the sense that tomographic measurement times were much shorter than previous tower-based radar imaging systems. This reduces the effects of temporal decorrelation during the measurement sequence. Tomograms from the multi-port VNA measurements were compared to tomograms reconstructed from replicated 2-port VNA measurements using mechanical relays to route VNA ports to antennas. Both image entropy and CNR were used as focusing quality metrics. Significant improvements in image quality were obtained for the multi-port VNA measurements at C-band for the measurements acquired during windy conditions. L-band tomograms showed minor improvements. Relative phase errors between antenna pairs were compensated for using an autofocus procedure based on image entropy minimization, which was sensitive to the wind-induced tree movement.

Contribution to paper:
I designed the antenna array geometry, implemented the radar system hardware (excluding tower-mounted components), implemented the software for automating the radar system, processed the data and produced the data analysis results. Interpretation of the results was done together with my co-authors. I prepared the manuscript together with L. M. H. Ulander.

6.2 Paper II

Temporal Survey of P- and L-band Polarimetric Backscatter in Boreal Forests

Before a robust calibration procedure for tomographic images was developed, backscatter and coherence were extracted from range profiles. In this paper, such P- and L-band backscatter and coherence time series from January to August 2017 are analysed. The C-band system was not installed during this time. The aim of the study was to investigate the relationships and correlations between the radar time series and time series of weather and *in situ* variables.

During winter, large drops in backscatter (4 to 10 dB) were observed at both bands and all polarisations as the air temperature dropped below 0°C. This was attributed to a decrease in dielectric constant due to both frozen soil and frozen trunk moisture. During the spring/summer growing season, the P-band backscatter exhibited diurnal variations, along with temperature and vapour pressure deficit (VPD). Diurnal variations did not seem to originate from changing stem water content due to a diurnally varying VPD. Instead, it seemed to occur due to diurnal variations in wind speed. This was believed to be a result of trees bending in the wind, disturbing the double-bounce scattering mechanism, lowering the co-polarised backscatter and increasing the cross-polarised backscatter. A further analysis based on tomography in Paper IV gave results that modify these conclusions. At L-band, only an increase in HV backscatter was observed during windy times. Backscatter variations on timescales of days to weeks were observed that appeared to be due to a very high VPD and little rainfall, resulting in water stress in the trees. This was especially apparent at HH for both frequency bands. No significant difference in observed backscatter was observed when considering dawn and dusk satellite overpass times only.

Temporal coherence time series at P- and L-band, extending over a two-month period in the summer of 2017, were also analysed. Co-polarised P-band temporal coherence was high (>0.9) during the entire two-month period, except during windy periods. HV coherence was high during the first month, after which it dropped after a period of water stress. P-band coherence was highest during night and early morning times when the wind speed was low, which are the most suitable times for repeat-pass observations by BIOMASS. L-band coherence was low after the first few hours of the reference measurement, strongly discouraging repeat-pass SAR observations at L-band.

Contribution to paper:
I monitored and maintained the radar system during measurements, processed the data, produced the data analysis results and prepared the manuscript. Interpretation of the results was done together with L. M. H. Ulander.

6.3 Paper III

Calibration of a Ground-Based Array Radar for Tomographic Imaging of Natural Media

This paper describes and validates the calibration procedure that is necessary for analysing tomographic images from BorealScat data. Three new procedures were developed. In each case, a mathematical model was developed to show the effects of the systematic errors in question and how they can be compensated for.

Firstly, a method for suppressing the effects of mutual antenna coupling without affecting the range resolution is described and validated. Strong mutual coupling, combined with a narrow bandwidth (such as the 30 MHz bandwidth at P-band), results in sidelobes in range profiles that distort the responses from the forest and trihedral corner reflector. Sidelobe suppression by applying a tapering window was not suitable since the resolution would be affected and the number of looks, which are already low at P-band, would be further reduced. The presented method is based on a line spectrum estimation method and has the effect of removing artefacts from tomographic images and exposing the trihedral corner reflector response from sidelobes without affecting the range resolution.

With the trihedral corner reflector's peak exposed in range profiles, the second method describes the use of this reflector response to calibrate magnitude and phase imbalances between antennas. These imbalances arise from unequal losses and propagation delays in cables between antennas. These errors have the effect of defocusing tomographic images. Mathematical relationships between transmit-receive antenna pairs are used to derive cross-polarisation calibration constants from co-polarisation calibration constants. This calibration step results in consistently well-focused tomographic images. The method is also robust to temporal variations in the magnitude of the reflector's response, which were observed to coincide with temperature and moisture variations.

After the reconstruction of focused tomographic images, the magnitude of each pixel in the image has a different systematic bias. This bias is a result of the antenna gain varying across the imaging plane and the resolution cell size increasing with distance from the antennas. A method for compensating for a pixel-dependent bias is described and validated. The method uses a simulation to estimate the energy of the impulse response corresponding to each pixel in a tomographic image. This step allows quantitative comparisons of the scattering contributions of the ground and the canopy, and also corrects for a bias in the coherence computed from a region of interest.

Contribution to paper:
I proposed and developed the mutual coupling suppression method. The magnitude and phase calibration method was suggested by S. Tebaldini. The impulse response compensation method was inspired by previous work by S. Tebaldini and L. M. H. Ulander. I developed the mathematical formulation in the paper and tested the methods on BorealScat data. I prepared the manuscript, which was finalized together with my co-authors.

6.4 Paper IV

Temporal Characteristics of P-band Tomographic Radar Backscatter of a Boreal Forest

With a robust tomographic calibration procedure in place, the temporal evolution of tomographic images could be studied. In this paper, backscatter time series extracted from P-band tomographic images are analysed. The time series extend over a period of two years. Time series of systematic variables are shown to demonstrate the temporal stability of the radar system. Also, a simulation is used to investigate how speckle variations affect P-band time series observations from the BorealScat radar. Three polarisation combinations were considered: HH, VV and VH. HV results were excluded from the analysis because of evidence of residual cross-talk.

Backscatter variations due to freeze/thaw cycles, seasonal changes, snow cover/melt, diurnal variations, rainfall and wind are analysed and discussed. Freeze/thaw backscatter variations (10 dB) were shown to originate mainly in the upper canopy of the forest. Apart from the effects of reduced canopy attenuation during freezing, backscatter from the ground decreased only in sustained frozen conditions. During nonfrozen conditions, the canopy backscatter was observed to be more stable than the ground or full forest backscatter for HH and VV. Cross-polarised backscatter was dominated by the canopy contribution, resulting in similar temporal variations for the two forest regions. No significant difference in backscatter distributions were seen when only considering dawn and dusk satellite overpass times, agreeing with the results from Paper II. No significant effects of snow were observed, although the site did not experience significant amounts of snow cover during the observation period. Different diurnal patterns in the canopy and ground were observed. These variations were small (1 dB) and, thus, careful consideration of speckle statistics was taken in the analysis. A daytime drop in canopy backscatter was connected with the reduction of the water content of tree tissues. The analysis suggested that strong winds during the summer had a similar effect, building on the interpretation given in Paper II. The diurnal backscatter patterns of the canopy and ground were different, a phenomenon which could not be explained using current knowledge of tree water transport dynamics.

Contribution to paper:
I processed the data, produced the data analysis results and prepared the manuscript. Interpretation of the results was done together with L. M. H. Ulander.

6.5 Paper V

Temporal Coherence in a Boreal Forest at P-, L- and C-band: A Tower-based Radar Study

While the backscatter variations observed in Paper IV are important for forest parameter estimation algorithms using SAR data, temporal coherence is important for the design of orbital patterns for spaceborne SAR missions. In this paper, the temporal coherence during a summer and winter period are analysed over timescales varying from seconds to weeks for P-, L- and C-band. Measures of temporal coherence were computed from two tomographic images acquired at different times. Tomographic images were used to provide a higher number of looks, not to investigate the coherence contributions from different heights within the forest.

P-band coherence was observed to be high over timescales necessary for repeat-pass interferometry, only being significantly disturbed by freezing temperatures. L-band coherence was more dependent on the time of day of acquisition, season and environmental conditions. The best L-band acquisition times were during the night and early morning during the summer when transpiration activity and convective winds were at their lowest. The probability of a high temporal coherence during other conditions were generally low for L-band. On average, C-band coherence was only observed to be high over temporal baselines of seconds and up to a few hours during summer nights. Examples of the temporal evolution of temporal coherence are shown. Temporal decorrelation is shown to occur during transpiration, wind, rain, freezing, thawing and sub-zero temperature variations.

The results show that the BIOMASS observation scheme is suitable for SAR interferometry and tomography during nonfrozen conditions. Repeat-pass interferometry is only consistently possible for L-band SARs during the night/dawn overpasses during the summer. Ideally, multiple SARs flying in close formation should be used at L- and C-band, with overpass times separated by hours and seconds, respectively, to reduce temporal decorrelation.

Contribution to paper:
I processed the data, produced the data analysis results and prepared the manuscript. Interpretation of the results was done together with L. M. H. Ulander.

7

Conclusions and future work

This thesis presents the design, implementation, evaluation and data analysis results for an experiment aimed at studying temporal characteristics of radar measurements in a boreal forest. The experiment emulated spaceborne SAR observations with a fixed observation geometry, allowing the study of temporal variations over a vast range of timescales.

A dedicated tower-based array radar, capable of tomographic imaging of natural media from P- to C-band, was implemented. This is the first ground-based tomographic system capable of operating over such a wide frequency range. The radar system is capable of receiving scattered fields using several antennas simultaneously, resulting in much shorter tomographic measurement times than previous ground-based tomographic radars. The short measurement times allowed for reconstructing focused tomograms during windy conditions. New signal processing techniques were developed for suppressing the effects of mutual antenna coupling, compensating for magnitude and phase imbalances between antennas in an array and for correcting the effects of space-variant resolution cells in tomographic images. Nevertheless, there was still evidence of cross-talk in the HV channel.

The largest variations in backscatter were due to freezing and thawing. Tomography allowed the separation of scattering contributions within the forest, showing that the majority of freeze/thaw backscatter variations were due to freezing in the upper canopy at P-band. With the absence of long-term variations due to soil moisture changes, the canopy backscatter was very stable with time during nonfrozen conditions. This supports the use of tomography and interferometric ground-notching for forest parameter estimation. The response of backscatter to wind and temperature during the summer indicated that backscatter was sensitive to water content variations within trees, although the exact relationship between tree water dynamics and the observed backscatter remains uncertain. Temporal variations of HH and VV backscatter were similar, being a mix of ground and canopy contributions. Cross-polarised backscatter was dominated by the canopy contribution, which showed similar temporal variations to the canopy contributions at HH and VV at P-band.

Temporal coherence was shown to be stable over periods long enough for repeat-pass tomography at P-band. L-band temporal coherence was observed to be more dependent on observation time of day and season, with generally low temporal coherences for temporal baselines exceeding a few hours. C-band temporal coherence was only consistently high over timescales of seconds. These observations support the observation strategy of BIOMASS, and strongly motivate the implementation of L- and C-band SAR constellations flying in close formation to minimise temporal decorrelation in interferometric and tomographic applications.

The results presented in this thesis come from a fraction of the full volume of collected data. Results from analysis of tomographic backscatter time series at L- and C-band and from Doppler measurements have not been published in peer-reviewed articles yet. The BorealScat radar instrument also features measurements at UHF-band (614 - 670 MHz), which are thus far unexplored. Time series data of tree radius and sap flow have been collected at the site and must be analysed to gain a better understanding of how tree water dynamics affects the radar backscatter.

With the forest slowly dying from an infestation of bark beetles, plans are underway to relocate the experiment setup to a different forest in Sweden, which is also equipped with a flux tower and a variety of sensors acquiring meteorological, hydrological and ecological data. Results from this thesis suggest that variables related to evapotranspiration may be sensed using radar. The additional variables available from the new forest site will allow a deeper study of the relationship between the energy and water balance in relation to radar measurements of forests.

References

Abtew, W. and A. Melesse (2013). Vapor Pressure Calculation Methods. *Evaporation and Evapotranspiration: Measurements and Estimations*. Dordrecht: Springer Netherlands, pp. 53–62.

Aghababaei, H. et al. (2020). Forest SAR tomography: principles and applications. *IEEE Geoscience and Remote Sensing Magazine*, vol. 8, no. 2, pp. 30–45.

Albinet, C. et al. (2012). TropiSCAT: a ground based polarimetric scatterometer experiment in tropical forests. *IEEE Journal of Selected Topics in Applied Earth Observations and Remote Sensing*, vol. 5, no. 3, pp. 1060–1066.

Albinet, C. et al. (2015). First results of AfriScat, a tower-based radar experiment in African forest. *International Geoscience and Remote Sensing Symposium (IGARSS), Milan, Italy, 26-31 July 2015*, pp. 5356–5358.

Albinet, C. et al. (2016). Measure of temporal variation of P-band radar cross section and temporal coherence of a temperate tree. *IEEE Transactions on Geoscience and Remote Sensing*, vol. 54, no. 11, pp. 6255–6264.

Alemohammad, S. H. et al. (2019). Soil and vegetation scattering contributions in L-band and P-band polarimetric SAR observations. *IEEE Transactions on Geoscience and Remote Sensing* , vol. 57, no. 11, pp. 8417–8429.

Askne, J. I. H. et al. (2013). Model-based biomass estimation of a hemi-boreal forest from multitemporal TanDEM-X acquisitions. *Remote Sensing*, vol. 5, no. 11, pp. 5574–5597.

Askne, J. I. H., M. J. Soja, and L. M. H. Ulander (2017). Biomass estimation in a boreal forest from TanDEM-X data, lidar DTM, and the interferometric water cloud model. *Remote Sensing of Environment*, vol. 196, pp. 265–278.

Askne, J. I. H. et al. (1997). C-band repeat-pass interferometric SAR observations of the forest. *IEEE Transactions on Geoscience and Remote Sensing*, vol. 35, no. 1, pp. 25–35.

Bamler, R. and P. Hartl (1998). Synthetic aperture radar interferometry. *Inverse Problems*, vol. 14, no. 4, R1–R54.

Banda, F. et al. (2020). The BIOMASS level 2 prototype processor: design and experimental results of above-ground biomass estimation. *Remote Sensing*, vol. 12, no. 6, pp. 1–28.

Billingsley, J. B. (2002). *Low-Angle Radar Land Clutter-Measurements and Empirical Models*. William Andrew Publishing/Noyes Publishing, Norwich.

Birrer, I. J. et al. (1982). σ^0 signature of the Amazon rain forest obtained from the Seasat scatterometer. *IEEE Transactions on Geoscience and Remote Sensing*, vol. GE-20, no. 1, pp. 11–17.

Bohren, C. F. and D. R. Huffman (1998). *Absorption and Scattering of Light by Small Particles*. John Wiley & Sons, New York, USA.

Borderies, P. et al. (2013). TropiSCAT: Final report. *European Space Agency (ESA), Paris, France, Tech. Rep. Contract No. 4000103506/11/NL/CT/FK*.

Bowes, B. G. (2010). *Trees and Forests, a Colour Guide: Biology, Pathology, Propagation, Silviculture, Surgery, Biomes, Ecology, and Conservation*. Taylor & Francis Group.

Brown, H. R. (2013). The theory of the rise of sap in trees: some historical and conceptual remarks. *Physics in Perspective*, vol. 15, no. 3, pp. 320–358.

Campbell, G. S. and J. M. Norman (1998). Conductances for Heat and Mass Transfer. *An Introduction to Environmental Biophysics*. New York, USA: Springer New York, pp. 87–111.

Čermák, J. et al. (2007). Tree water storage and its diurnal dynamics related to sap flow and changes in stem volume in old-growth Douglas-fir trees. *Tree physiology*, vol. 27, no. 2, pp. 181–198.

Chiu, T. and K. Sarabandi (1999). Electromagnetic scattering interaction between a dielectric cylinder and a slightly rough surface. *IEEE Transactions on Antennas and Propagation*, vol. 47, no. 5, pp. 902–913.

Chu, C. R. et al. (2008). Transient response of sap flow to wind speed. *Journal of Experimental Botany*, vol. 60, no. 1, pp. 249–255.

Cloude, S. R. (2006). Polarization coherence tomography. *Radio Science*, vol. 41, no. 4, RS4017.

Cloude, S. R. and K. P. Papathanassiou (1998). Polarimetric SAR interferometry. *IEEE Transactions on Geoscience and Remote Sensing*, vol. 36, no. 5, pp. 1551–1565.

Crang, R., S. Lyons-Sobaski, and R. Wise (2018). *Plant Anatomy: A Concept-Based Approach to the Structure of Seed Plants*. Springer International Publishing.

d'Alessandro, M. M. et al. (2020). Interferometric ground cancellation for above ground biomass estimation. *IEEE Transactions on Geoscience and Remote Sensing (Early Access)*, pp. 1–10.

Damour, G. et al. (2010). An overview of models of stomatal conductance at the leaf level. *Plant, Cell & Environment*, vol. 33, no. 9, pp. 1419–1438.

Daudet, F. A. et al. (1999). Wind speed and leaf boundary layer conductance variation within tree crown: consequences on leaf-to-atmosphere coupling and tree functions. *Agricultural and Forest Meteorology*, vol. 97, no. 3, pp. 171–185.

Davidson, M. et al. (2018). Copernicus L-band SAR Mission Requirements Document, ESA-EOPSM-CLIS-MRD-3371. *Earth and Mission Science Division, European Space Agency*.

De Loor, G. P., P. Hoogeboom, and E. P. W. Attema (1982). The Dutch ROVE Program. *IEEE Transactions on Geoscience and Remote Sensing*, vol. GE-20, no. 1, pp. 3–11.

Dixon, H. H and J Joly (1894). On the ascent of sap. *Proceedings of the Royal Society of London*, vol. 57, pp. 3–5.

Dobson, M. C. et al. (1992). Dependence of radar backscatter on coniferous forest biomass. *IEEE Transactions on Geoscience and Remote Sensing*, vol. 30, no. 2, pp. 412–415.

El Idrissi Essebtey, S. et al. (2020). Temporal decorrelation of tropical dense forest at C-band: first insights from the TropiScat-2 experiment. *IEEE Geoscience and Remote Sensing Letters*, vol. 17, no. 6, pp. 928–932.

Entekhabi, D. et al. (2014). *SMAP handbook–soil moisture active passive: Mapping soil moisture and freeze/thaw from space*. JPL Publication; Pasadena, CA, USA.

Eriksson, L. E. B. et al. (2003). Multitemporal JERS repeat-pass coherence for growing-stock volume estimation of Siberian forest. *IEEE Transactions on Geoscience and Remote Sensing*, vol. 41, no. 7 PART I, pp. 1561–1570.

ESA (2012). *Report for Mission Selection: BIOMASS, ESA SP-1324/1 (3 volume series)*. European Space Agency, Noordwijk, The Netherlands.

Fransson, J. E. S., F. Walter, and L. M. H. Ulander (2000). Estimation of forest parameters using CARABAS-II VHF SAR data. *IEEE Transactions on Geoscience and Remote Sensing*, vol. 38, no. 2, pp. 720–727.

Frey, O. and E. Meier (2011). 3-D time-domain SAR imaging of a forest using airborne multibaseline data at L- and P-bands. *IEEE Transactions on Geoscience and Remote Sensing*, vol. 49, no. 10, pp. 3660–3664.

Frey, O., C. L. Werner, and A. Wiesmann (2015). Tomographic profiling of the structure of a snow pack at X-/Ku-Band using SnowScat in SAR mode. *2015 European Radar Conference, EuRAD 2015 - Proceedings*, pp. 21–24.

Friedlingstein, P. et al. (2019). Global carbon budget 2019. *Earth System Science Data*, vol. 11, no. 4, pp. 1783–1838.

Friesen, J. et al. (2007). Spatial and seasonal patterns of diurnal differences in ERS Scatterometer soil moisture data in the Volta Basin, West Africa. *IAHS Publication*, vol. 316, pp. 47–55.

Frolking, S. et al. (2011). Tropical forest backscatter anomaly evident in SeaWinds scatterometer morning overpass data during 2005 drought in Amazonia. *Remote Sensing of Environment*, vol. 115, no. 3, pp. 897–907.

Gauthier, S. et al. (2015). Boreal forest health and global change. *Science*, vol. 349, no. 6250, pp. 819–822.

Goff, John A. (1946). Low-pressure properties of water-from 160 to 212°F. *Transactions of the American Society of Heating and Ventilating Engineers*, vol. 52, pp. 95–121.

Hagberg, J. O., L. M. H. Ulander, and J. I. H. Askne (1995). Repeat-pass SAR interferometry over forested terrain. *IEEE Transactions on Geoscience and Remote Sensing*, vol. 33, no. 2, pp. 331–340.

Hajnsek, I. et al. (2008). BioSAR 2007: Technical assistance for the development of airborne SAR and geophysical measurements during the BioSAR 2007 experiment: Final report. *European Space Agency (ESA), Paris, France, Tech. Rep. Contract No. 20755/07/NL/CB*.

Hallikainen, M. T. et al. (1985). Microwave dielectric behavior of wet soil-Part 1: empirical models and experimental observations. *IEEE Transactions on Geoscience and Remote Sensing* , vol. GE-23, no. 1, pp. 25–34.

Herzog K. M.and Häsler, R. and R. Thum (1995). Diurnal changes in the radius of a subalpine Norway spruce stem: their relation to the sap flow and their use to estimate transpiration. *Trees* , vol. 10, no. 2, pp. 94–101.

Hirons, A. D. and P. A. Thomas (2017). Tree Water Relations. *Applied Tree Biology*. John Wiley & Sons, Ltd. Chap. 6, pp. 239–259.

Hobbs, S. et al. (2018). G-CLASS:H2O, A mission to observe and understand processes of the daily water cycle over land, ESA ref.: CEE10/008. *European Space Agency*.

Hölttä, T. et al. (2013). Fluxes of Carbon, Water and Nutrients. *Physical and Physiological Forest Ecology*. Dordrecht: Springer Netherlands, pp. 225–328.

Homer, J., I. D. Longstaff, and G. Callaghan (1996). High resolution 3-D SAR via multi-baseline interferometry. *International Geoscience and Remote Sensing Symposium (IGARSS), Lincoln, Nebraska, USA, 27.31 May 1996*, pp. 796–798.

Hufford, G. (1991). A model for the complex permittivity of ice at frequencies below 1 THz. *International Journal of Infrared and Millimeter Waves*, vol. 12, no. 7, pp. 677–682.

Hussin, Y. A., R. M. Reich, and R. M. Hoffer (1991). Estimating slash pine biomass using radar backscatter. *IEEE Transactions on Geoscience and Remote Sensing*, vol. 29, no. 3, pp. 427–431.

IEEE (2003). IEEE Standard Letter Designations for Radar-Frequency Bands. *IEEE Std 521-2002 (Revision of IEEE Std 521-1984)*, pp. 1–3.

Israelsson, H., J. I. H. Askne, and R. Sylvander (1994). Potential of SAR for forest bole volume estimation. *International Journal of Remote Sensing*, vol. 15, no. 14, pp. 2809–2826.

Israelsson, H. et al. (1997). Retrieval of forest stem volume using VHF SAR. *IEEE Transactions on Geoscience and Remote Sensing*, vol. 35, no. 1, pp. 36–40.

Jarvis, P. G. (1976). The interpretation of the variations in leaf water potential and stomatal conductance found in canopies in the field. *Philosophical Transactions of the Royal Society of London. B, Biological Sciences*, vol. 273, no. 927, pp. 593–610.

Jarvis, P. G. and K. G. McNaughton (1986). "Stomatal Control of Transpiration: Scaling Up from Leaf to Region". Ed. by A. MacFadyen and E. D. Ford. Vol. 15. Advances in Ecological Research. Academic Press, pp. 1–49.

Kalinkevich, A. A. (2013). On measuring the permittivity of "living" wood for microwave remote sensing. *Journal of Communications Technology and Electronics*, vol. 58, no. 9, pp. 919–925.

Koskinen, J. T. et al. (2001). The seasonal behavior of interferometric coherence in boreal forest. *IEEE Transactions on Geoscience and Remote Sensing*, vol. 39, no. 4, pp. 820–829.

Krieger, G. et al. (2007). TanDEM-X: a satellite formation for high-resolution SAR interferometry. *IEEE Transactions on Geoscience and Remote Sensing*, vol. 45, no. 11, pp. 3317–3340.

Kristensson, G. (2016). *Scattering of Electromagnetic Waves by Obstacles*. SciTech Publishing, Edison, New Jersey, USA.

Lagergren, F. and A. Lindroth (2002). Transpiration response to soil moisture in pine and spruce trees in Sweden. *Agricultural and forest meteorology*, vol. 112, no. 2, pp. 67–85.

Landsberg, J., R. Waring, and M. Ryan (2017). Water relations in tree physiology: where to from here? *Tree Physiology*, vol. 37, no. 1, pp. 18–32.

Lavalle, M., M. Simard, and S. Hensley (2012). A temporal decorrelation model for polarimetric radar interferometers. *IEEE Transactions on Geoscience and Remote Sensing*, vol. 50, no. 7, pp. 2880–2888.

Le Toan, T. et al. (1992). Relating forest biomass to SAR data. *IEEE Transactions on Geoscience and Remote Sensing*, vol. 30, no. 2, pp. 403–411.

Lee, J. and E. Pottier (2009). *Polarimetric radar imaging: from basics to applications*. CRC press.

Lee, S. et al. (2013). Quantification of temporal decorrelation effects at L-band for polarimetric SAR interferometry applications. *IEEE Journal of Selected Topics in Applied Earth Observations and Remote Sensing*, vol. 6, no. 3, pp. 1351–1367.

Lindroth, A. and P. Crill (2011). Hydrology and Biogeochemistry of Boreal Forests. *Forest Hydrology and Biogeochemistry: Synthesis of Past Research and Future Directions*. Ed. by D. F. Levia, D. Carlyle-Moses, and T. Tanaka. Dordrecht: Springer Netherlands, pp. 321–339.

López-Dekker, P. et al. (2019). Harmony: an Earth Explorer 10 mission candidate to observe land, ice, and ocean surface dynamics. *International Geoscience and Remote Sensing Symposium (IGARSS), Yokohama, Japan, 28 July to 2 August 2019*, pp. 8381–8384.

Luojus, K. et al. (2020). *IDEAS-QA4EO Snow product calibration and validation + FMI Sodankylä snow Cal/Val Infrastructure*. URL: `https://earth.esa.int/eogateway/documents/20142/1484253/Advanced-algorithms-and-Cal-Val-protocols-for-satellite-based-Snow-products.pdf`. (accessed: 2020-08-01).

Mätzler, C., ed. (2006). *Thermal Microwave Radiation: Applications for Remote Sensing*. Electromagnetic Waves. Institution of Engineering and Technology.

Mätzler, C. and U. Wegmüller (1987). Dielectric properties of freshwater ice at microwave frequencies. *Journal of Physics D: Applied Physics*, vol. 20, no. 12, pp. 1623–1630.

Mavrovic, A. et al. (2018). Dielectric characterization of vegetation at L band using an open-ended coaxial probe. *Geoscientific Instrumentation, Methods and Data Systems*, vol. 7, no. 3, pp. 195–208.

McCulloh, K. A. et al. (2014). The dynamic pipeline: hydraulic capacitance and xylem hydraulic safety in four tall conifer species. *Plant, Cell & Environment*, vol. 37, no. 5, pp. 1171–1183.

McDonald, K. C., R. Zimmermann, and J. S. Kimball (2002). Diurnal and spatial variation of xylem dielectric constant in Norway spruce (*Picea abies* [L.] Karst.) as related to microclimate, xylem sap flow, and xylem chemistry. *IEEE Transactions on Geoscience and Remote Sensing*, vol. 40, no. 9, pp. 2063–2082.

McDonald, K. C. et al. (1999). Automated instrumentation for continuous monitoring of the dielectric properties of woody vegetation: system design, implementation, and selected in situ measurements. *IEEE Transactions on Geoscience and Remote Sensing*, vol. 37, no. 4, pp. 1880–1894.

Minh, D. H. T. et al. (2013). Ground-based array for tomographic imaging of the tropical forest in P-band. *IEEE Transactions on Geoscience and Remote Sensing*, vol. 51, no. 8, pp. 4460–4472.

Minh, D. H. T. et al. (2015). The impact of temporal decorrelation on BIOMASS tomography of tropical forests. *IEEE Geoscience and Remote Sensing Letters*, vol. 12, no. 6, pp. 1297–1301.

Minh, D. H. T. et al. (2016). SAR tomography for the retrieval of forest biomass and height: cross-validation at two tropical forest sites in French Guiana. *Remote Sensing of Environment*, vol. 175, pp. 138–147.

Mironov, V. L. et al. (2019). Experimental analysis and empirical model of the complex permittivity of five organic soils at 1.4 GHz in the temperature range from -30°C to 25°C. *IEEE Transactions on Geoscience and Remote Sensing*, vol. 57, no. 6, pp. 3778–3787.

Moghaddam, M., S. Durden, and H. A. Zebker (1994). Radar measurement of forested areas during OTTER. *Remote Sensing of Environment*, vol. 47, no. 2, pp. 154–166.

Moghaddam, M. and S. Saatchi (1995). Analysis of scattering mechanisms in SAR imagery over boreal forest: results from BOREAS ’93. *IEEE Transactions on Geoscience and Remote Sensing*, vol. 33, no. 5, pp. 1290–1296.

Moghaddam, M. and S. Saatchi (1999). Monitoring tree moisture using an estimation algorithm applied to SAR data from BOREAS. *IEEE Transactions on Geoscience and Remote Sensing*, vol. 37, no. 2, pp. 901–916.

Moghaddam, M., S. Saatchi, and R. H. Cuenca (2000). Estimating subcanopy soil moisture with radar. *Journal of Geophysical Research: Atmospheres*, vol. 105, no. D11, pp. 14899–14911.

Monteith, J. and M. Unsworth (2013). *Principles of Environmental Physics : Plants, Animals, and the Atmosphere*. 4th edition. Elsevier Science & Technology.

Moreira, A. et al. (2013). A tutorial on synthetic aperture radar. *IEEE Geoscience and Remote Sensing Magazine*, vol. 1, no. 1, pp. 6–43.

Moreira, A. et al. (2015). Tandem-L: a highly innovative bistatic SAR mission for global observation of dynamic processes on the Earth’s surface. *IEEE Geoscience and Remote Sensing Magazine*, vol. 3, no. 2, pp. 8–23.

Morrison, K. and J. Bennett (2014). Tomographic profiling - a technique for multi-incidence-angle retrieval of the vertical SAR backscattering profiles of biogeophysical targets. *IEEE Transactions on Geoscience and Remote Sensing*, vol. 52, no. 2, pp. 1350–1355.

Morrison, K., J. Bennett, and S. Solberg (2013). Ground-based C-band tomographic profiling of a conifer forest stand. *International Journal of Remote Sensing*, vol. 34, no. 21, pp. 7838–7853.

Morrison, R. L., M. N. Do, and D. C. Munson (2007). SAR image autofocus by sharpness optimization: a theoretical study. *IEEE Transactions on Image Processing*, vol. 16, no. 9, pp. 2309–2321.

Nagarajan, K. et al. (2014). Automated L-band radar system for sensing soil moisture at high temporal resolution. *IEEE Geoscience and Remote Sensing Letters*, vol. 11, no. 2, pp. 504–508.

Narayanan, R. M., D. W. Doerr, and D. C. Rundquist (1992). Temporal decorrelation of X-band backscatter from wind-influenced vegetation. *IEEE Transactions on Aerospace and Electronic Systems*, vol. 28, no. 2, pp. 404–412.

O'Neill, P. E. et al. (2006). "Multi-sensor microwave soil moisture remote sensing: NASA's combined radar/radiometer (ComRAD) system". *2006 IEEE MicroRad*, pp. 50–54.

Oliver, C. and S. Quegan (2004). *Understanding Synthetic Aperture Radar Images*. SciTech Publishing.

Pan, Y. et al. (2011). A large and persistent carbon sink in the world's forests. *Science*, vol. 333, no. 6045, pp. 988–993.

Pardini, M. et al. (2012a). On the estimation of forest vertical structure from multibaseline polarimetric SAR data. *International Geoscience and Remote Sensing Symposium (IGARSS), Munich, Germany, 22-27 July 2012*, pp. 3443–3446.

Pardini, M. et al. (2012b). Phase calibration of multibaseline SAR data based on a minimum entropy criterion. *International Geoscience and Remote Sensing Symposium (IGARSS), Munich, Germany, 22-27 July 2012*, pp. 5198–5201.

Parkin, Gary W. (2008). Water Budget In Soil. *Encyclopedia of Soil Science*. Ed. by Ward Chesworth. Dordrecht: Springer Netherlands, pp. 811–813.

Pastorino, M. (2010). *Microwave Imaging*. John Wiley & Sons, Incorporated, Hoboken.

Peplinski, N. R., F. T. Ulaby, and M. C. Dobson (1995). Dielectric properties of soils in the 0.3-1.3-GHz range. *IEEE Transactions on Geoscience and Remote Sensing*, vol. 33, no. 3, pp. 803–807.

Pfautsch, S., T. Hölttä, and M. Mencuccini (2015). Hydraulic functioning of tree stems - fusing ray anatomy, radial transfer and capacitance. *Tree Physiology*, vol. 35, no. 7, pp. 706–722.

Pfautsch, S. et al. (2015). Phloem as capacitor: radial transfer of water into xylem of tree stems occurs via symplastic transport in ray parenchyma. *Plant Physiology*, vol. 167, no. 3, pp. 963–971.

Pulliainen, J. T., M. Engdahl, and M. T. Hallikainen (2003). Feasibility of multi-temporal interferometric SAR data for stand-level estimation of boreal forest stem volume. *Remote Sensing of Environment*, vol. 85, no. 4, pp. 397–409.

Pulliainen, J. T., L. Kurvonen, and M. T. Hallikainen (1999). Multitemporal behavior of L- and C-band SAR observations of boreal forests. *IEEE Transactions on Geoscience and Remote Sensing*, vol. 37, no. 2, pp. 927–937.

Quegan, S. et al. (2019). The European Space Agency BIOMASS mission: measuring forest above-ground biomass from space. *Remote Sensing of Environment*, vol. 227, pp. 44–60.

Raicu, V. and Y. Feldman (2015). *Dielectric relaxation in biological systems: physical principles, methods, and applications.* Oxford University Press.

Ranson, K. J. and S. Guoqing (1994). Mapping biomass of a northern forest using multifrequency SAR data. *IEEE Transactions on Geoscience and Remote Sensing*, vol. 32, no. 2, pp. 388–396.

El-rayes, M. A. and F. T. Ulaby (1987). Microwave dielectric spectrum of vegetation-Part I: experimental observations. *IEEE Transactions on Geoscience and Remote Sensing*, vol. GE-25, no. 5, pp. 541–549.

Regan, A., P. Silvestrin, and D. Fernandez (2016). Sentinel convoy: synergetic earth observation with satellites flying in formation with European operational missions. *European Space Agency, (Special Publication) ESA SP*, vol. SP-740.

Reigber, A. and A. Moreira (2000). First demonstration of airborne SAR tomography using multibaseline L-band data. *IEEE Transactions on Geoscience and Remote Sensing*, vol. 38, no. 5, pp. 2142–2152.

Richards, J. A., G. Sun, and D. S. Simonett (1987). L-band radar backscatter modeling of forest stands. *IEEE Transactions on Geoscience and Remote Sensing*, vol. GE-25, no. 4, pp. 487–498.

Rott, H. et al. (2017). SESAME: a single-pass interferometric Sentinel-1 companion SAR mission for monitoring geo- and biosphere dynamics. *International Geoscience and Remote Sensing Symposium (IGARSS), Fort Worth, USA, 23-28 July 2017*, pp. 107–110.

Saatchi, S. and M. Moghaddam (2000). Estimation of crown and stem water content and biomass of boreal forest using polarimetric SAR imagery. *IEEE Transactions on Geoscience and Remote Sensing*, vol. 38, no. 2, pp. 697–709.

Salas, W. A. et al. (1994). Temporal and spatial variations in dielectric constant and water status of dominant forest species from New England. *Remote Sensing of Environment*, vol. 47, no. 2, pp. 109–119.

Santoro, M. and O. Cartus (2018). Research pathways of forest above-ground biomass estimation based on SAR backscatter and interferometric SAR observations. *Remote Sensing*, vol. 10, no. 4, pp. 1–23.

Satake, M. and H. Hanado (2004). Diurnal change of Amazon rain forest σ^0 observed by Ku-band spaceborne radar. *IEEE Transactions on Geoscience and Remote Sensing*, vol. 42, no. 6, pp. 1127–1134.

Schulz, T. J. (2007). Optimal sharpness function for SAR autofocus. *IEEE Signal Processing Letters*, vol. 14, no. 1, pp. 27–30.

Sellin, A. (1994). Sapwood–heartwood proportion related to tree diameter, age, and growth rate in *Picea abies*. *Canadian Journal of Forest Research*, vol. 24, no. 5, pp. 1022–1028.

Sephton, Tony and Alex Wishart (2013). TOPOLEV and C-PARAS. *Distributed Space Missions for Earth System Monitoring*. Ed. by Marco D'Errico. New York, NY: Springer New York, pp. 473–508.

Sevanto, S., T. Hölttä, and N. M. Holbrook (2011). Effects of the hydraulic coupling between xylem and phloem on diurnal phloem diameter variation. *Plant, Cell & Environment*, vol. 34, no. 4, pp. 690–703.

Sevanto, S. et al. (2002). Time lags for xylem and stem diameter variations in a Scots pine tree. *Plant, Cell & Environment*, vol. 25, no. 8, pp. 1071–1077.

Shteinshleiger, V. B. et al. (1997). Obtaining high resolution in transionospheric space-borne VHF-band SAR for Earth remote sensing. *IEE Conference Publication* , no. 449, pp. 268–272.

Sihvola, A. (1999). *Electromagnetic Mixing Formulas and Applications*. Electromagnetic Waves. Institution of Engineering and Technology.

Smith-Jonforsen, G., L. M. H. Ulander, and X. Luo (2005). Low VHF-band backscatter from coniferous forests on sloping terrain. *IEEE Transactions on Geoscience and Remote Sensing*, vol. 43, no. 10, pp. 2246–2260.

Smith, G. and L. M. H. Ulander (2000). A model relating VHF-band backscatter to stem volume of coniferous boreal forest. *IEEE Transactions on Geoscience and Remote Sensing*, vol. 38, no. 2, pp. 728–740.

Soja, M. J., H. J. Persson, and L. M. H. Ulander (2015). Estimation of forest biomass from two-level model inversion of single-pass InSAR data. *IEEE Transactions on Geoscience and Remote Sensing*, vol. 53, no. 9, pp. 5083–5099.

Soja, M. J., G. Sandberg, and L. M. H. Ulander (2013). Regression-based retrieval of boreal forest biomass in sloping terrain using P-band SAR backscatter intensity data. *IEEE Transactions on Geoscience and Remote Sensing*, vol. 51, no. 5, pp. 2646–2665.

Solimini, D. (2016). *Understanding Earth Observation: The Electromagnetic Foundation of Remote Sensing*. Springer International Publishing.

Steele-Dunne, S. C., J. Friesen, and N. van de Giesen (2012). Using diurnal variation in backscatter to detect vegetation water stress. *IEEE Transactions on Geoscience and Remote Sensing*, vol. 50, no. 7, pp. 2618–2629.

Steffen, W. et al. (2015). Planetary boundaries: guiding human development on a changing planet. *Science*, vol. 347, no. 6223.

Steppe, K., F. Sterck, and A. Deslauriers (2015). Diel growth dynamics in tree stems: linking anatomy and ecophysiology. *Trends in Plant Science*, vol. 20, no. 6, pp. 335–343.

Sun, G., D. S. Simonett, and A. H. Strahler (1991). A radar backscatter model for discontinuous coniferous forests. *IEEE Transactions on Geoscience and Remote Sensing*, vol. 29, no. 4, pp. 639–650.

Tebaldini, S. (2009). Algebraic synthesis of forest scenarios from multibaseline PolInSAR data. *IEEE Transactions on Geoscience and Remote Sensing*, vol. 47, no. 12, pp. 4132–4142.

Tebaldini, S. and L. Ferro-Famil (2017). SAR tomography from bistatic single-pass interferometers. *International Geoscience and Remote Sensing Symposium (IGARSS), Fort Worth, USA, 23-28 July 2017*, pp. 133–136.

Tebaldini, S. and A. Monti Guarnieri (2010). On the role of phase stability in SAR multibaseline applications. *IEEE Transactions on Geoscience and Remote Sensing*, vol. 48, no. 7, pp. 2953–2966.

Tebaldini, S. and F. Rocca (2012). Multibaseline polarimetric SAR tomography of a boreal forest at P- and L-Bands. *IEEE Transactions on Geoscience and Remote Sensing*, vol. 50, no. 1, pp. 232–246.

Tebaldini, S. et al. (2015). Phase calibration of airborne tomographic SAR data via phase center double localization. *IEEE Transactions on Geoscience and Remote Sensing*, vol. 54, no. 3, pp. 1775–1792.

Tebaldini, S. et al. (2016). Imaging the internal structure of an alpine glacier via L-band airborne SAR tomography. *IEEE Transactions on Geoscience and Remote Sensing*, vol. 54, no. 12, pp. 7197–7209.

Thomas, S. C. and A. R. Martin (2012). Carbon content of tree tissues: A synthesis. *Forests*, vol. 3, no. 2, pp. 332–352.

Tice, A. R., P. B. Black, and R. L. Berg (1989). Unfrozen water contents of undisturbed and remolded Alaskan silt. *Cold Regions Science and Technology*, vol. 17, no. 2, pp. 103–111.

Torgovnikov, G. (1993). *Dielectric properties of wood and wood-based materials*. Springer Science & Business Media.

Torres, R. et al. (2012). GMES Sentinel-1 mission. *Remote Sensing of Environment*, vol. 120, pp. 9–24.

Torres, R. et al. (2017). Sentinel-1 SAR system and mission. *2017 IEEE Radar Conference, Seattle, USA, 8-12 May 2017*, pp. 1582–1585.

Touzi, R. et al. (1999). Coherence estimation for SAR imagery. *IEEE Transactions on Geoscience and Remote Sensing*, vol. 37, no. 1, pp. 135–149.

Truong-Loï, M., S. Saatchi, and S. Jaruwatanadilok (2015). Soil moisture estimation under tropical forests using UHF radar polarimetry. *IEEE Transactions on Geoscience and Remote Sensing*, vol. 53, no. 4, pp. 1718–1727.

Tyree, M. T. and M. H. Zimmermann (2002). *Xylem Structure and the Ascent of Sap*. Springer Berlin Heidelberg.

Ulaby, F. T. (1975). Radar response to vegetation. *IEEE Transactions on Antennas and Propagation*, vol. 23, no. 1, pp. 36–45.

Ulaby, F. T. et al. (2014). *Microwave radar and radiometric remote sensing*. University of Michigan Press Ann Arbor.

Ulaby, F. T. and R. P. Jedlicka (1984). Microwave dielectric properties of plant materials. *IEEE Transactions on Geoscience and Remote Sensing*, vol. GE-22, no. 4, pp. 406–415.

Ulaby, F. T. and E. A. Wilson (1985). Microwave attenuation properties of vegetation canopies. *IEEE Transactions on Geoscience and Remote Sensing*, vol. GE-23, no. 5, pp. 746–753.

Ulander, L. M. H. (1991). Accuracy of using point targets for SAR calibration. *IEEE Transactions on Aerospace and Electronic Systems*, vol. 27, no. 1, pp. 139–148.

Ulander, L. M. H. et al. (2011). BioSAR 2010: Technical assistance for the development of airborne SAR and geophysical measurements during the BioSAR 2010 experiment: Final report. *European Space Agency (ESA), Paris, France, Tech. Rep. Contract No. 4000102285/10/NL/JA/ef.*

Ulander, L. M. H. et al. (2016). Borealscat: a tower experiment for understanding temporal changes in P- and L-band backscattering from a Boreal forest. *European Space Agency, (Special Publication) ESA SP*, vol. SP-740.

van Emmerik, T. et al. (2017). Water stress detection in the Amazon using radar. *Geophysical Research Letters*, vol. 44, no. 13, pp. 6841–6849.

Villard, L. and T. Le Toan (2015). Relating P-band SAR intensity to biomass for tropical dense forests in hilly terrain: γ^0 or t^0? *IEEE Journal of Selected Topics in Applied Earth Observations and Remote Sensing*, vol. 8, no. 1, pp. 214–223.

Watanabe, M. et al. (2015). Multitemporal fluctuations in L-band backscatter from a Japanese forest. *IEEE Transactions on Geoscience and Remote Sensing*, vol. 53, no. 11, pp. 5799–5813.

Wegmüller, Urs (1990). The effect of freezing and thawing on the microwave signatures of bare soil. *Remote Sensing of Environment*, vol. 33, no. 2, pp. 123–135.

Wu, S. T. (1987). Potential application of multipolarization SAR for pine-plantation biomass estimation. *IEEE Transactions on Geoscience and Remote Sensing*, vol. 25, no. 3, pp. 403–409.

Yun Shao et al. (2003). Effect of dielectric properties of moist salinized soils on backscattering coefficients extracted from RADARSAT image. *IEEE Transactions on Geoscience and Remote Sensing*, vol. 41, no. 8, pp. 1879–1888.

Zebker, H. A. and J. Villasenor (1992). Decorrelation in interferometric radar echoes. *IEEE Transactions on Geoscience and Remote Sensing*, vol. 30, no. 5, pp. 950–959.

Zhu, X. X. and R. Bamler (2010). Tomographic SAR inversion by L_1 -norm regularization-The compressive sensing approach. *IEEE Transactions on Geoscience and Remote Sensing*, vol. 48, no. 10, pp. 3839–3846.

Zimmermann, R. et al. (1995). Xylem dielectric constant, water status, and transpiration of young Jack Pine (*Pinus banksiana* Lamb.) in the southern boreal zone of Canada. *International Geoscience and Remote Sensing Symposium (IGARSS), Firenze, Italy, 10-14 July 1995*, vol. 2, pp. 1006–1008.

Zweifel, R., J. P. Böhm, and R. Häsler (2002). Midday stomatal closure in Norway spruce—reactions in the upper and lower crown. *Tree Physiology*, vol. 22, no. 15-16, pp. 1125–1136.

Zweifel, R. and R. Häsler (2000). Frost-induced reversible shrinkage of bark of mature subalpine conifers. *Agricultural and Forest Meteorology*, vol. 102, no. 4, pp. 213–222.

Zweifel, R. and R. Häsler (2001). Dynamics of water storage in mature subalpine *Picea abies*: temporal and spatial patterns of change in stem radius. *Tree physiology*, vol. 21, no. 9, pp. 561–569.

Zweifel, R., H. Item, and R. Häsler (2001). Link between diurnal stem radius changes and tree water relations. *Tree physiology*, vol. 21, no. 12-13, pp. 869–877.